Biomaterials Science

ROYAL SOCIETY OF CHEMISTRY

PAPER

Published on 05 August 2026
Licensed under CC-BY 4.0

Check for updates

Cite this: *Biomater. Sci.*, 2026, **14**, 5246

Towards therapeutic applications of nanobody-Fc constructs: comparative analysis of Fc receptor binding and macrophage activation

Miglė Stančiauskaitė, [a,c] Mantvydas Usvaltas,[c] Kristina Mašalaitė, [b] Asta Lučiūnaitė*[b,c] and Ieva Plikusiene *[a,c]

Nanobodies (Nbs) are new and promising tools for a variety of applications, including their use in medicine, although their functional activity and encounter with immune cells are still not well characterized. Our goal was to study the properties of Nbs coupled with the human IgG1 antibody Fc fragment (Nb-Fc), including their interaction with antigens, Fc receptors (FcRs), and professional phagocytes: macrophages. In our research, we employed a combination of two surface-sensitive methods: spectroscopic ellipsometry (SE) and quartz crystal microbalance with dissipation (QCM-D). It enabled the quantitative investigation of interaction kinetics between human FcγRI (CD64) and immune complexes (IC) formed by the severe acute respiratory syndrome coronavirus 2 (SARS-CoV-2) spike protein Wuhan variant (SCoV2-S) and specific Nb-Fc, as well as the optical and mechanical properties of the formed layers. Human THP-1 macrophage cell culture was used to analyze antigen and IC induced inflammatory response, antigen presentation-related processes, as well as chemokine CCL2/CCR2 and CCL5/CCR5 axes. Our investigated Nb-Fcs had a high affinity for SCoV2-S that was comparable to that of the natural human antibody CR3022. ICs formed by Nb-Fcs also interacted with FcRs in a similar way to CR3022. One of the investigated Nb-Fcs distinguished itself by its very high affinity and formed relatively the largest ICs. Interestingly, only ICs formed by the other Nb-Fcs influenced cellular response. We found increased cell surface expression of CD83. This molecule plays a regulatory role in antigen presentation and is involved in the resolution of inflammation following infection. In addition, we did not find any increase in other investigated markers in THP-1 macrophages, including the inflammatory response. Overall, our data demonstrate that Nb-Fcs can be applied in a similar manner to conventional human antibodies, considering their properties.

Received 7th April 2026,
Accepted 1st August 2026

DOI: 10.1039/d6bm00509h

rsc.li/biomaterials-science

Introduction

Nanobodies (Nbs) or so-called single domain antibodies are produced by camelids, such as llamas and alpacas. Their small size, enhanced affinity and high stability lead to a better performance of Nbs for targeting specific regions of viruses or cells, offering potential advantages such as lower immunogenicity and easier engineering for enhanced functionality.[1] For example, Nbs have been explored for targeting viruses, like SARS-CoV-2, enhancing cancer immunotherapy and treating diseases such as hepatitis and osteoarthritis, by targeting specific inflammatory pathways and delivering drugs directly to the joint.[2–4] Nbs have also demonstrated anti-inflammatory effects *in vitro* through the reduction of the inflammatory cytokine interleukin-1 beta.[5] Compared to short peptides, Nbs have also demonstrated superior performance in blocking SCoV2-S binding to the cell *via* the ACE2 receptor and preventing virus entry into the host cell, indicating the prevention of infection.[6,7] In contrast to conventional antibodies, Nbs can be easily engineered from existing libraries and remodelled for assay purposes, potentially helping to overcome fast mutational evolution of viruses. Nbs and their bioconjugates can be applied in standard immunoassays and label-free biosensing. For example, in western blotting Nbs can detect denatured targets and cryptic epitopes on SARS-CoV-2 spike variants.[8] Nb-Fc constructs have also shown superior performance to the monovalent version of Nbs; WA2.22-Fc exhibited an EC_{50} of 10.1 ± 1.5 nM on binding pathological tau aggregates, while another study demonstrated a better SARS-CoV-2 neutralisation effect, highlighting the possible Fc contribution in certain circumstances.[9,10] Nb-Fc was also applied in optical

[a]*Faculty of Chemistry and Geosciences, Institute of Chemistry, Vilnius University, Naugarduko g. 24, LT-03225 Vilnius, Lithuania. E-mail: ieva.plikusiene@chgf.vu.lt*
[b]*Institute of Biotechnology, Life Sciences Center, Vilnius University, Sauletekio av. 7, LT-10257 Vilnius, Lithuania. E-mail: asta.luciunaite@bti.vu.lt*
[c]*State Research Institute Center for Physical and Technological Sciences, Sauletekio av. 3, Vilnius, Lithuania*

This journal is © The Royal Society of Chemistry 2026

biosensing techniques, such as biolayer interferometry (BLI) and photonic bimodal waveguide (BiMW) interferometry, to detect monkeypox A35R membrane protein and SCoV2-S RBD, reaching K_D values in the nano- to subnanomolar range.[11,12] As Fc fusion adds an Fc fragment to Nbs and enables their interaction with Fc receptors (FcRs), it is important to characterise how Nb-Fc immune complexes (ICs) interact with these receptors in comparison to conventional IgG.

FcRs are critical components of the immune system that mediate communication between antibodies and immune effector cells, modulating processes such as phagocytosis, antibody-dependent cellular cytotoxicity, and inflammatory responses.[13,14] These receptors recognise the Fc region of antibodies bound to antigens, forming ICs that trigger receptor clustering and downstream signalling cascades. The diverse family of FcRs, including FcγR, FcαR, FcεR, and FcμR, is expressed on distinct immune cell types and they exhibit varied affinity and specificity for antibody isotypes.[15–18] Understanding how FcRs interact with immune complexes at the molecular and kinetic levels is essential not only for advancing fundamental immunology, but also for improving therapeutic antibody design, vaccine efficacy, and immune diagnostics.[19]

Recent advancements in biosensing, including surface plasmon resonance (SPR), biolayer interferometry (BLI), NanoBiT bioluminescence assays, high-speed atomic force microscopy and bio-nanocapsule scaffolds, have transformed the investigation of IC–FcR interactions by providing real-time, label-free, high-sensitivity platforms that quantify binding affinities and yield complementary information on FcR binding kinetics, receptor–ligand structural changes, and molecular mechanisms.[20–26] Among these, solution-based systems such as NanoBiT have emerged as powerful tools that minimise surface-related artefacts, supporting sensitive, high-throughput and real-time detection of receptor interactions. Insights derived from these biosensing studies emphasise the crucial roles of Fc glycosylation, hinge region flexibility and antigen-induced allosteric modulation in determining receptor affinity and functional outcomes.[27–30] Despite this progress, translational applications remain limited by difficulties in isolating native immune complexes and achieving physiological receptor specificity, which motivates the integration of advanced biosensing with molecular modelling and multiplex detection strategies to uncover FcR mechanisms and guide next-generation therapeutic antibody and biosensor diagnostic design.[31–33]

The thermodynamic properties of IC formation can be related to inflammation, as shown in our previous work highlighting the need for real-time, label-free characterisation of IC kinetics.[34] Surface-sensitive and non-destructive methods such as spectroscopic ellipsometry (SE) and quartz crystal microbalance with dissipation (QCM-D) enable such analysis. SE detects changes in the polarization state of reflected light, which allows the calculation of the thickness and refractive index of protein monolayers, while QCM-D provides hydrated surface mass density and viscoelastic properties. Altogether, these methods give complementary information on protein monolayer formation, binding kinetics, structure, hydration and orientation in real time and their application to antibody–antigen monolayers was recently presented in our reports.[35–38]

The aim of our study was to investigate the application of biosensing techniques for characterising IC–FcγRI interactions in relation to immune cell responses. By employing real-time and label-free biosensing-based methods, SE and QCM-D, we compared ICs formed by natural human antibodies with ICs formed by Nb-Fc, as Nbs are promising tools for various medical applications and immunoassays, but there is still a lack of a comprehensive analysis of their functional activity. The relevance of the IC–FcγRI interaction, determined by biophysical descriptions of biosensing results, was consolidated through immune cell-based immunoassays.

Materials and methods

Materials

11-Mercaptoundecanoic acid (11-MUA, 98%), 1-ethyl-3-(3-dimethylaminopropyl)carbodiimide (EDC, ≥98%), *N*-hydroxysuccinimide (NHS, 98%), ethanolamine (ETA) (≥99%), and phosphate-buffered saline (PBS) tablets were purchased from Sigma Aldrich. Methanol (99.9%) and glycine (≥99%) were purchased from Carl Roth GmbH & Co (Karlsruhe, Germany). Recombinant SCoV2-S glycoprotein (cat#22-S2SOM1-TCg-F, SARS-CoV-2 Spike glycoprotein Wuhan variant expressed as secreted trimeric protein in mammalian (hamster) CHO cells) was purchased from Baltymas (Vilnius, Lithuania). Surface plasmon resonance (SPR) sensors were purchased from XanTec bioanalytics (Duesseldorf, Germany). Gold-coated QCM-D quartz crystal sensor discs with a resonance frequency of 4.95 MHz and a diameter of 14 nm were purchased from Biolin Scientific (Gothenburg, Sweden). Roswell Park Memorial Institute 1640 medium (RPMI, cat#61870044), live cell imaging solution (cat#A59688DJ), fetal bovine serum (FBS; cat#10500-064), penicillin/streptomycin (cat#15140122), and Dulbecco's Phosphate Buffered Saline (PBS; cat#14190250) were obtained from Gibco, Thermo Fischer Scientific. Cell culture plates: T75 culture flasks and cell culture treated EasYFlasks (cat#156499) were from Nunc, Thermo Fischer Scientific; TPP multi-well tissue culture plates (cat# 92012, cat#92024, cat#92048) were from TPP Techno Plastic Products AG; μ-Slide 8 Well (cat#80826) was from Ibidi. Phorbol 12-myristate 13-acetate (PMA, cat# P1585-1MG), dialysis tubes D-Tube Dialyzer Mini, MWCO 12–14 kDa, (cat#71505, Millipore), LDH assay: Cytotoxicity Detection Kit PLUS (LDH) (cat#4744934001, CYTODET-RO Roche) was obtained from Sigma-Aldrich by Merck. Dimethylsulfoxide (DMSO; cat#A3672) was from PanReac AppliChem and ITW Reagents. pHrodo iFL Green STP ester dye (cat# P36013), deep red CellMask membrane stain (cat#C10046), UltraPure DNase/RNase-free distilled water (cat#10977035), 7AAD (cat#00-6993-50), and Hoechst33342 (cat#H3570) were from Invitrogen, Thermo Fischer Scientific. PBS/EDTA (cat#9152.1), containing 0.046% EDTA, Bovine serum albumin (BSA, Albumin Fraction V, cat#1ETA.3), Tween-20 (cat# 9127.1) and sulphuric acid

(H_2SO4, cat#X873.1) were from CarlRoth. Human TruStain FcX™ (Fc receptor blocking solution, cat#422302) was from Biolegend. Flow cytometry antibodies against human antigens: anti-CD86-AlexaFluor 488 (cat#53-0869-42, clone B7-2, Invitrogen, Thermo Fischer Scientific), anti-CCR2-PE (cat#357206, clone K036C2, Biolegend), anti-CD83-AlexaFluor 647 (cat#305316, clone HB15e, Biolegend), and anti-CCR5-AlexaFluor 405 (cat#FAB184V-100UG, Clone #45529, R&D Systems). Isotype controls: unstained mouse IgG2b isotype control (Cat#MAB004, Clone # 20116, R&D Systems); PE mouse IgG2a, κ Isotype Ctrl clone MOPC-173 (cat# 400214, Biolegend); mouse IgG2b kappa isotype control (eBMG2b) Alexa Fluor 488, eBioscience (Cat# 53-4732-80, Invitrogen, Thermo Fischer Scientific); Alexa Fluor® 647 Mouse IgG1, κ Isotype Ctrl (cat#400130, Biolegend). Human antibodies anti-spike (S) protein in PBS with 0.02% Proclin 300 were from AbsoluteAntibodies, clones: anti-COVID-19 & SARS-CoV S glycoprotein #CR3022 (Product Code: Ab01680-10.0); human IgG1-Fc fusion anti-spike protein (RBD): Sb#14 *(Product Code: Ab02012-10.159), Sb#15 (Product Code: Ab02013-10.159), Sb#68 (Product Code: Ab02017-10.159); C_{stock} = 1.0 mg ml^{-1}. Recombinant SARS-CoV-2 WT spike protein – full-length trimeric ectodomain, C_{stock} = 1.0 mg ml^{-1} (SCoV2-S product, cat#20-S2S-TCg-F) was from Baltymas.

TIRE and SE/QCM-D measurement setup

SCoV-2 spike interaction with Nb-Fcs and human IgG1 was monitored using a spectroscopic ellipsometer M-2000X (J.A. Woollam, USA) in total internal reflection (TIRE) configuration at 70° angle of incidence across 200–1000 nm. A 70° BK7 prism was coupled to the gold-coated SPR sensor disc using an index-matching liquid and mounted to a custom Teflon liquid-handling chamber. Surface modification and rinsing steps were monitored *in situ*; ellipsometric parameters Ψ and Δ were recorded as functions of time and wavelength (λ).

Immune complex binding to CD64 and competitive Nb assays were evaluated using an integrated QCM-D/SE instrument. QCM-D (QSense Explorer, Biolin Scientific, Sweden; 5 MHz) was used to monitor seven harmonics for viscoelastic modelling. For combined measurements, the QCM-D and SE module was used. The measurement chamber above the gold sensor held 100 μL, and solutions were pumped through PTFE tubing at 1.0 mL min^{-1} with a peristaltic pump (Cole-Parmer GmbH, Germany). The temperature was controlled at 20 °C. ΔF and ΔD were acquired using QSoft401 to follow the kinetics of CD64 or SCoV2-S immobilization and affinity interactions allowing the derivation of adsorbed-layer mass, thickness, and viscoelastic parameters. SE measurements were obtained with an M-2000X (J.A. Woollam, USA) at 65° across 200–1000 nm. Ellipsometric parameters Ψ and Δ were acquired for each interaction and analysed in CompleteEASE software.

Surface modification with 11-MUA

The gold-coated QCM-D sensor discs were cleaned 2 times by sonication in methanol for 2 minutes. The sensor was then dried and immediately immersed in a 1 mM solution of 11-MUA in methanol for 22 h to form a self-assembled monolayer (SAM). Following incubation, the sensor was rinsed thoroughly with methanol and dried under a gentle stream of nitrogen. The sensor with SAM was installed in the SE/QCM-D module, which was then filled with PBS (pH 7.4) and kept for over 30 minutes to form a baseline. Carboxyl groups of 11-MUA were activated by injection of an equal volume solution of 0.1 M NHS and 0.4 M EDC and kept in the cell for 15 minutes. A PBS (pH 7.4) rinse was then applied for 5 minutes to re-establish the baseline.

Immobilisation of the SCoV-2 spike protein and immunocomplex formation with monoclonal antibodies

To evaluate the kinetics of IC formation, a 333 nM solution of SCoV2-S in PBS was injected into the chamber and incubated for 60 minutes to enable immobilisation on the activated surface. After incubation, the chamber was rinsed with PBS to remove unbound SCoV2-S. A 1 M ethanolamine hydrochloride solution (pH 8.5) was then injected for 10 minutes to deactivate residual activated carboxyl groups, followed by a PBS rinse to remove the blocking agent. After a stable baseline was established, 100 nM solutions of nanobodies SB14, SB15, and SB68, as well as the human IgG antibody CR3022, were injected and held for 60 minutes. Following each interaction with monoclonal antibodies, the sensor surface was regenerated with 10 mM glycine hydrochloride (pH 2) to disrupt bound protein interactions with SCoV2-S, remove residual antibodies, and prepare the surface for subsequent measurements.

Immobilization of CD64 and affinity measurements for IC interactions

For FcγRI/IC interaction measurements, a 300 nM solution in PBS (pH 7.4) of FcR CD64 was injected into the QCM-D cell and randomly immobilized onto the sensor surface. After 80 minutes of incubation, SE and QCM-D measurements were in the steady state. To remove the residual unbound receptor and confirm baseline stability, the sensor surface was rinsed with PBS for 10 minutes.

ICs were prepared by diluting SCoV2-S and the nanobody (or antibody) of choice to a final complex concentration of 100 nM and incubating the mixture in a dry-block at 37 °C for 45 min. After equilibrating to room temperature, the ICs were injected into the QCM-D chamber and allowed to associate with the immobilized FcγRI for 120 min. Unbound ICs were rinsed by flowing PBS for 5–10 min. The sensor surface was regenerated with 10 mM glycine (pH 2) for 5 minutes, followed by a 10-minute PBS rinse to verify the regeneration quality and terminate the measurement. For each different IC, a new setup with a fresh QCM-D sensor was used to achieve the most accurate kinetic measurements. Each IC/CD64 interaction was measured in two separate experiments using independently prepared sensor surfaces.

Cell culture

Macrophages derived by the THP-1 monocytic cell line were used for the study. The cells were kindly given by Dr Linas

 This journal is © The Royal Society of Chemistry 2026

Mazutis (Life Sciences Center, Vilnius University). THP-1 monocytes were cultivated in RPMI 1640 cell culture medium supplemented with 10% FBS and antibiotics 1%/1% penicillin/streptomycin – complete medium. The cells were differentiated into macrophages using 100 ng mL^{-1} PMA for 48 h, and then the medium was changed to fresh complete medium and incubated for 24 h, a resting period. The differentiated cells were treated in serum-free RPMI 1640 medium supplemented with penicillin/streptomycin for 24 h in all cases, if otherwise mentioned. 83.3 nM of SCoV2-S and 27.7 nM of antibody were used for the treatment. ICs were formed by incubating SCoV2-S and the antibody in cell culture medium for 30 min at 37 °C. Cell culture medium served as the control treatment. After the treatment, the cells were used for analysis, and cell culture supernatants were collected and centrifuged at 600*g* for 10 min to remove cellular debris. Supernatants were stored at −70 °C and used for enzyme-linked immunosorbent assay (ELISA).

For flow cytometry analysis and collection of cell culture supernatants, THP-1 macrophages were grown in TPP multi-well tissue culture plates, with 0.125 million cells in 24-well plates (cat# 92012, TPP Techno Plastic Products AG). Cells grown in 96-well ibiTreat μ-plates (cat#89626, Ibidi) were used for wide-field microscopy analysis; cells were seeded at a density of 0.08 million per well. Cells grown in 8-well ibiTreat μ-slides (cat#80826, Ibidi) were used for confocal microscopy analysis; cells were seeded at a density of 0.0625 million per well.

Evaluation of cell viability

Cell viability was measured according to their metabolic activity using the lactate dehydrogenase (LDH) detection assay (cat#11644793001, Roche, Sigma-Aldrich by Merck). LDH is released during cell death. LDH was detected in the cell culture supernatant according to the manufacturer's protocol. Briefly, 50 μl of freshly collected supernatant was mixed with 50 μl of prepared assay solution (components 1 and 2 were mixed at a ratio of 1 : 45) and incubated for 30 min at 37 °C. Then, 50 μl of stop solution was added and the absorbance was measured at 490 nm using the Multiskan GO microplate spectrophotometer (Thermo Fisher Scientific Oy, Finland). As a positive control, Triton X-100 solution, already prepared and included in the kit, was used. The percentage of change from control (100%) was calculated from the measured optical densities.

Cytokine detection by ELISA

Secreted cytokines were detected by ELISA in THP-1 macrophage cell culture following the manufacturer's protocols. ELISA-based cytokine detection kits were used: human IL-1 beta uncoated ELISA kit (cat#88-7261-86), human TNF alpha uncoated ELISA kit (cat#88-7346-86), human MCP-1/CCL2 uncoated ELISA kit (cat#88-7399-22), and human IL-10 uncoated ELISA kit (cat#88710688) were from Invitrogen, Thermo Fisher Scientific; human CCL5/RANTES DuoSet ELISA kit (cat#DY278) was from R&D systems. Supernatant dilution up to 10 times was used for the assays.

SCoV2-S and its IC phagocytosis analysis by microscopy

To investigate phagocytosis, THP-1 macrophages were treated for 3 h with SCoV2-S labelled with pHrodo Green dye or ICs formed by labelled SCoV2-S and unlabelled Nb-Fc. pHrodo Green dye is fluorescent at low pH and allows the detection of the protein signal in lysosomes. After the treatment live cells were used for microscopy analysis.

SCoV2-S was labelled with pHrodo iFL Green STP ester dye according to the manufacturer's protocol. Briefly, a 100 μg vial of the pHrodo Green amine-reactive dye was dissolved in 15 μL of DMSO to prepare ~10 mM stock solution. A 10-molar excess of dye stock solution was added to the SCoV2-S solution, which had a concentration of 1 mg ml^{-1}, in phosphate-buffered saline (PBS). The prepared mixture was incubated for 60 min at room temperature. SCoV2-S-pHrodo Green conjugate was purified using dialysis overnight at 4 °C. D-Tube Dialyzer of 12-14 kDa (cat#71505-3, Merck Millipore) and Dulbecco's Phosphate Buffered Saline (DPBS; cat#14190250, Gibco, Thermo Fisher Scientific) solution of 10× volume of sample volume were used for the dialysis. Purified protein conjugates were stored at −20 °C, in the same manner as unlabelled SCoV2-S.

In the case of confocal microscopy, cells were examined with a Leica TCS SP8 laser scanning microscope (Leica Microsystems, Germany). Thirty minutes before the treatment termination, cells were stained with Deep Red CellMask Membrane Stain (1 : 1000). After the staining cell culture medium was replaced with Live Cell Imaging Solution. 184.52 × 184.52 μm *XY* size 3D images with a pixel size of 180.38 nm (format 1024 × 1024) were taken using a 63×/1.40 oil-objective. *Z*-stack images had a *z*-size of 17.04 μm and 58 frames with a *z*-step size of 0.3 μm (system optimized). 3D images were acquired using the following filters at the same time, in non-sequential scan mode: in excitation 500 nm/emission 505–585 nm (Green pHrodo, detector HyD1), excitation 641 nm/emission 646–784 nm (Deep Red, detector HyD3). The mean fluorescence intensity per cell of each photo was calculated using the ImageJ program.

In the case of wide-field microscopy, cells were examined with a Nikon Ti2-E fully automated fluorescence microscope (Nikon Corporation, Japan). Cells were treated with SCoV2-S-pHrodo Green or ICs for 3 h. In the case of actin polymerisation inhibition, cytochalasin D was added 30 min before the treatment. Thirty minutes before the treatment termination, the cell nuclei were stained with Hoechst 33342. Then, the medium was changed to live cell imaging solution. The photos were taken with a 20× objective in automatic scan mode of selected wells (9 photos per well) with Nikon NIS-Elements software in two channels: DAPI – Hoechst 33342 and FITC – pHrodo Green. Nikon NIS-Elements software was also used for the analysis of the count cell number and mean fluorescence intensity (MFI) per well. MFI was divided by the cell count according to the nuclear count to measure the intensity per cell, which was used for statistical analysis.

To prove FcR-dependent ICs phagocytosis, FcR blocking was used. Ten min before exposure to SCoV2-S-pHrodo Green

and ICs, human Fc receptor blocking solution (cat#58948, Cell Signaling Technology) was added at a concentration of 10 μg per 1 million cells. This solution contains a modified form of human IgG1 that blocks human Fc receptors. 30 min before the end of the treatment, nuclei were stained with Hoechst 33342, and the medium was changed to DPBS. Live cells were analysed using a wide-field microscope, a Nikon Ti2-E, in two channels: DAPI (Hoechst 33342) and FITC (pHrodo Green). The photos were taken in automatic scan mode with an 40× objective. Large images of 8 × 8 fields (2673.23 × 2673.23 microns) were generated. Nikon NIS-Elements software was also used for analysis to count cell numbers (according to cell nuclei) and determine fluorescence intensities per well.

Acquired images were processed using ImageJ (Wayne Rusband; National Institute of Health, USA). For image preparation the appropriate pseudo-colour was added at images of 8-bit format. Then, the images were converted to the RGB colour format, and brightness and contrast were adjusted equally to all images per channel.

SCoV2-S and its IC phagocytosis analysis by flow cytometry

To investigate phagocytosis, THP-1 macrophages were treated for 3 h with SCoV2-S labelled with pHrodo Green dye or ICs formed by labelled SCoV2-S and unlabelled Nb-Fc. 30 min before exposure to SCoV2-S and ICs, cells were incubated with the phagocytosis inhibitor cytochalasin D. After treatment, live cells were analysed by flow cytometry. They were washed with DPBS, and PBS/EDTA solution was added. The cells were collected using cell scrapers, centrifuged at 300*g* for 10 min, then resuspended in PBS/EDTA and centrifuged again. Before the analysis, 3 μl per 100 μl of 7AAD dye was added for 5 minutes. The cells were analysed using a BD FACS Symphony A1 flow cytometer (Becton, Dickinson and Company, USA). Data were analysed with the FlowJo program. Cell populations were selected based on FSC-A and SSC-A plots. Then, duplicates were discriminated using FSC-H and FSC-A plots. Live 7-AAD-negative cells were used for the analysis. The percentage of pHrodo Green-positive cells was calculated and referred to the phagocytosed cells.

Cell activation marker detection by flow cytometry

After cell treatment, they were washed with DPBS and PBS/EDTA solution was added. The cells were collected using cell scrapers and centrifuged at 300*g* for 10 min, and then resuspended in a blocking solution: DPBS supplemented with 2% BSA, Fc receptor blocking solution (1 : 50), and unstained mouse IgG2b isotype control (1 : 100). After 15 min incubation, specific antibodies (1 : 100) were added directly to the blocking solution. One panel of specific antibodies (anti-CD86-AlexaFluor 488, anti-CCR2-PE, anti-CD83-AlexaFluor 647 and anti-CCR5-AlexaFluor 405) or respective isotype controls was used (final volume 100 μL per sample). After 25 min incubation, the cell viability dye 7-AAD was added to the stains (3 μL per 100 μL) and incubated for another 5 min. Then, the cells were centrifuged at 300*g* for 5 min and resuspended in PBS/EDTA solution. The cells were analysed using BD FACS Symphony A1 flow cytometer (Becton, Dickinson and Company, USA). Data were analysed with the FlowJo program. Cell populations were selected according to FSC-A and SSC-A plots. Then duplicates were discriminated using FSC-H and FSC-A plots. Live 7-AAD negative cells were used for the analysis. The mean fluorescence intensity of the measured signal or the percentage of positive cells were calculated for further statistical analysis.

Statistical analysis

Statistical analysis was performed with GraphPad Prism 10.6.1 (GraphPad Software, Inc., La Jolla, CA). The data in the figures are represented as individual data points using bar graphs (mean and standard deviation) or box plots (showing minimum, first quartile, median, third quartile and maximum). In independent experiments N means the number of independent cell culture preparations, and n is the technical repeats. A normality test was conducted to determine if the values originated from a Gaussian distribution. Statistical comparisons of vehicle controls *versus* treatment were performed with ANOVA in conjunction with a Tukey's multiple comparison test or an unpaired Student's t-test. Differences with a p value less than 0.05 were statistically significant: $*p < 0.05$, $**p < 0.01$, $***p < 0.001$, $****p < 0.0001$.

Results and discussion

Results

Real-time immune complex formation measurements. TIRE measurements were performed in order to investigate the binding kinetics between SCoV2-S and selected Nb-Fcs Sb14, Sb15 and Sb68 nanobodies, as well as the natural human IgG1 antibody CR3022 (Fig. 1A). The kinetic curves and calculated kinetic parameters showed the differences between Sb14, Sb15 and Sb68 (Fig. 1 and Table 1). It was observed that the SCoV2-S interaction with Nb-Fc Sb14 resulted in the lowest K_D of 2.10×10^{-11} M, while Sb15, Sb68 and CR3022 interactions with SCoV2-S yielded K_D in the same magnitude of ^−10. These data show that Sb14 was of the highest affinity to SCoV2-S.

A similarity was observed between Sb15/SCoV2-S and CR3022/SCoV2-S IC formation, displaying highly similar K_D, although association (k_a) and dissociation (k_d) rate constants of the SCoV2-S interaction with Sb15 were both ∼1.5 times higher (Table 1). Regarding k_d, the values were of varying magnitude, ranging from the highest to lowest in the order Sb15 > CR3022 > Sb68 > Sb14. Kinetic data allowed us to conclude that Nb-Fc interactions with SCoV2-S are comparable to those of the natural human IgG1 antibody CR3022.

Dry surface mass densities (Γ^{SE}) were derived from the refractive index change in time during Nb-Fc and antibody interactions with SCoV2-S (Fig. 1B). For Sb14, Γ^{SE} showed the highest value of 54.14 ng cm^{-2}. The second highest value of Γ^{SE} was that for the CR3022 layer (45.10 ng cm^{-2}). Despite the same molar mass between Nb-Fcs, Sb15 and Sb68 formed layers of lower surface mass density than that of Sb14, being 39.06 and 30.68 ng cm^{-2}, respectively. Our results show that

 This journal is © The Royal Society of Chemistry 2026

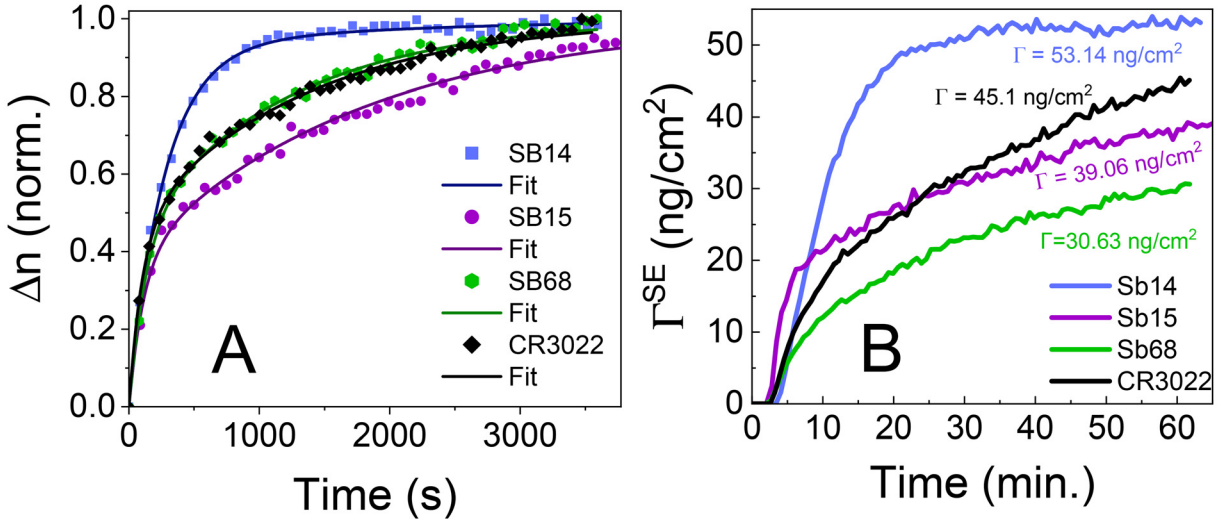


Fig. 1 (A) Time-resolved kinetics of the SCoV2-S interaction with Sb14 (dotted orange), Sb15 (purple), Sb68 (green) and CR3022 (blue); black curves show fitting results using a two-step kinetic binding model. (B) Dry surface mass density evolution in time for Sb14 (orange), Sb15 (purple), Sb68 (green) and CR3022 (blue) monolayers formed during the interaction with SCoV2-S.

Table 1 Kinetic parameters of SCoV2-S immobilization and its interaction with Sb14, Sb15, Sb68 and CR3022 derived from two step binding fit (Fig. 1A solid curves). Here k_a – association rate, k_r – stable complex formation rate, k_d – dissociation rate, K_A – equilibrium association, and K_D – equilibrium dissociation (affinity) constants

Interaction	k_a (M^{-1} s^{-1})	k_r (s^{-1})	k_d (s^{-1})	K_A (M^{-1})	K_D (M)
11-MUA/SCoV2-S	1.62×10^4	1.05×10^{-5}	4.26×10^{-5}	3.82×10^8	2.62×10^{-9}
SCoV2-S/Sb14	3.45×10^4	1.91×10^{-6}	7.24×10^{-7}	4.76×10^{10}	2.10×10^{-11}
SCoV2-S/Sb15	7.70×10^4	8.39×10^{-6}	2.83×10^{-5}	2.72×10^9	3.68×10^{-10}
SCoV2-S/Sb68	3.87×10^4	6.39×10^{-6}	1.16×10^{-6}	3.34×10^9	2.99×10^{-10}
SCoV2-S/CR3022	4.81×10^4	7.41×10^{-6}	1.96×10^{-5}	2.46×10^9	4.07×10^{-10}

the highest affinity Nb-Fc Sb14 covered the SCoV2-S layer to the largest extent.

Immune complex real-time interaction with FcγRI

QCM-D measurements. QCM-D measurements allowed us to compare the changes in frequency and dissipation (ΔF and ΔD, respectively) for immobilization of FcγRI (CD64) and its interaction with different ICs. For random immobilization of CD64, ΔF and ΔD were similar throughout the experiments, resulting in −21.2 Hz and 0.9 for the 7th harmonic, respectively (Fig. 2A and B). Differences emerged when comparing ICs formed from different Nb-Fcs and SCoV2-S, as well as the SCoV2-S/CR3022 complex. Between ICs formed by Nb-Fcs SCoV2-S/Sb14 achieved the biggest ΔF of −21.7 Hz upon interaction with the immobilized FcγRI (Fig. 2C).

A lower response of −17.9 Hz was observed for the Sb15/SCoV2-S complex (Fig. 2D), and an intermediate change in ΔF was recorded for Sb68/SCoV2-S IC (Fig. 2E). For Nb-Fc/SCoV2-S IC, changes in ΔF were smaller compared to the IC formed from the human antibody CR3022 and SCoV2-S (Fig. 2I). This is to be expected as Nbs used in these experiments only contain the Fc part and VHH domains. Regarding ΔD across ICs of Nb-Fc interactions with the FcγRI receptor, Sb14/SCoV2-S reached an intermediate ΔD of 1.5 for the 7th harmonic, Sb68/SCoV2-S IC reached a ΔD of 2.0, while the lowest ΔD (as well as ΔF) was for Sb15/SCoV2-S IC with ΔD = 1.2 after 120 minutes of interaction with CD64 and PBS wash. As expected, ΔD for the CR3022/SCoV2-S IC interaction with FcγRI was higher than that for Nb-Fc/SCoV2-S complexes. Conventional IgG1 antibodies, being heavier and larger in size, also carry more entrapped PBS with them, thereby increasing the ΔD of the formed layer.

Plotting ΔF *versus* ΔD from QCM-D measurements (Fig. S1) allowed us to observe monolayer formation. For viscoelastic monolayers, there was a change in both D and F, resulting in a positive slope of the line as the softness of the monolayer increases with thickness. It was noticed that before PBS wash the IC interaction with CD64 behaviour was similar for all cases (Fig. S1). A slightly curved line for lower harmonics indicates IC reorganization further from the sensor surface, as the volume closer to the surface (9th and 11th harmonic) displays a more constant change with the formed layer. On comparing the slopes of the 7th harmonic it was observed that for SCoV-2/Sb14 and SCoV-2/Sb15 the k value was 0.079 and for SCoV-2/Sb68 and SCoV-2/CR3022 it was 0.095 and 0.100, respectively. This indicates that the latter two IC layers exhibited slightly higher viscoelasticity.

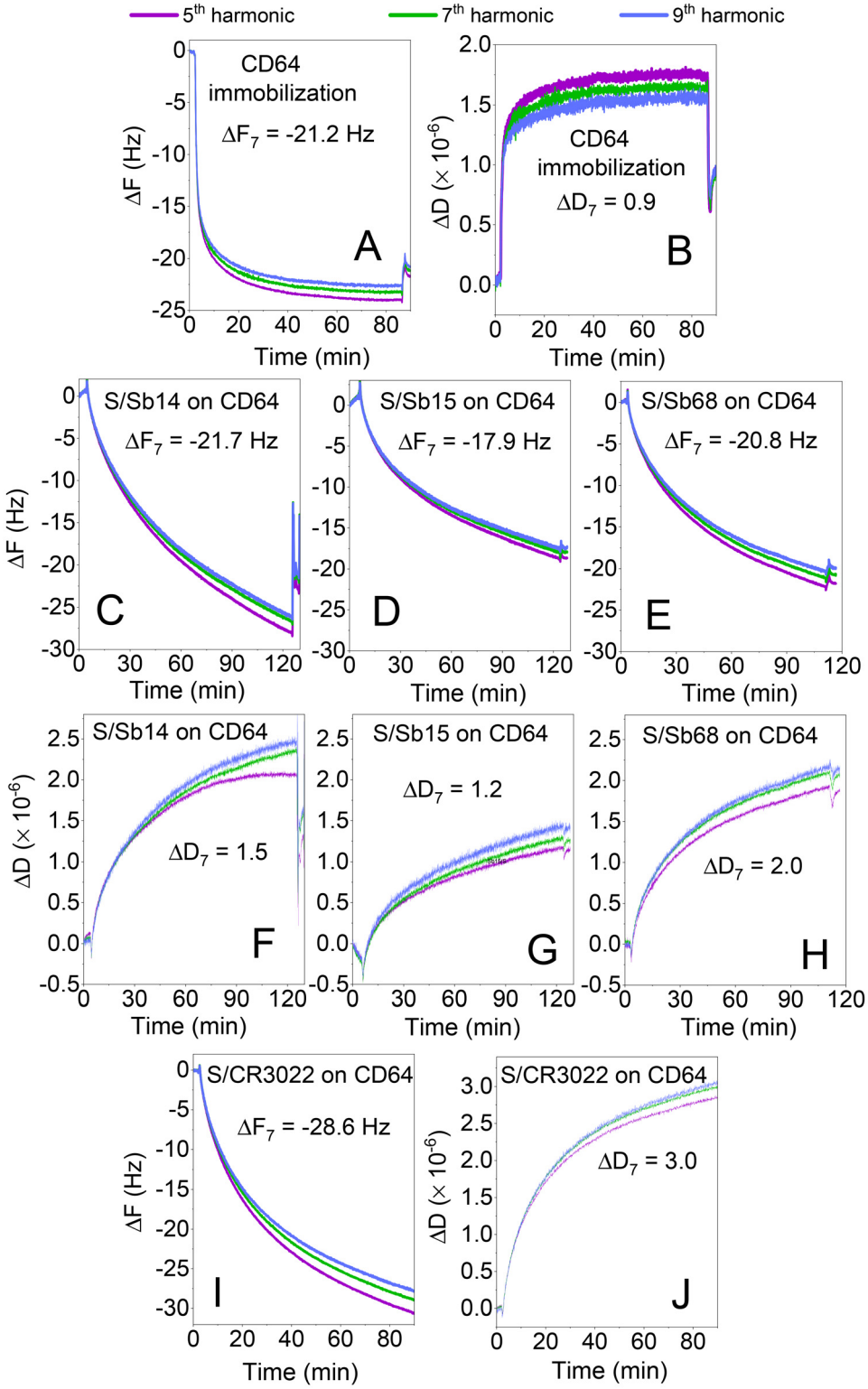


Fig. 2 ΔF and ΔD evolution in time of 5th, 7th and 9th harmonics for CD64 immobilization (A and B) and its interaction with S/Sb14 IC (C and F), S/Sb15 IC (D and G), S/Sb68 IC (E and H) and S/CR3022 IC (J and K). S – SCoV2-S.

These measurements overall show that Sb14 exhibited the most notable SE signal change among Nb-Fcs while binding to SCoV2-S, and the resulting ScoV2-S/Sb14 engagement with FcγRI was comparable to the human IgG1 antibody CR3022 QCM-D signal. A signal of similar intensity was observed for SCoV2-S/Sb68 on CD64, and overall, all investigated Nb-Fc ICs

 This journal is © The Royal Society of Chemistry 2026

effectively interacted with CD64, although slight differences in ΔF and ΔD lead to further investigation and comparison of binding kinetics.

SE measurements and modelling of thermodynamic properties. SE measurements allowed for tracking the change in the refractive index (n) over time during the formation of the FcγRI monolayer and the interaction with IC. Monolayer thicknesses were calculated by applying mathematical modelling using a two-step kinetic model.[37,39] For the monolayer of immobilized CD64, the thickness was 3.22–3.53 nm throughout all experiments. For layers of ICs upon interaction with FcγRI, the Sb14/SCoV2-S layer showed d = 21.9 nm, Sb15/SCoV2-S was the thinnest layer, being 18.05 nm, and for the Sb68/SCoV2-S layer the thickness was 20.69 nm. The IC of CR3022/SCoV2-S showed a thickness of 30 nm, in compliance with its bigger size and previously mentioned lower shifts of ΔF from the QCM-D results. The kinetic curve of FcγRI receptor immobilization is presented in Fig. 3A1.

Varying results were observed for IC interactions with the FcγRI receptor. SCoV2-S/Sb68 IC (Fig. 3D1) displayed the highest K_D of 1.092×10^{-9}, while SCoV2-S/Sb14 (Fig. 3B1) and especially SCoV2-S/Sb15 (Fig. 3C1) exhibited K_D very similar to that of SCoV2-S/CR3022 IC (Fig. 3E1). Similarities between SCoV2-S/Sb14, SCoV2-S/Sb15 and SCoV2-S/CR3022 repeated throughout k_r and k_d, while the association rate constant k_a for the SCoV2-S/CR3022 was ~8 times higher.

Surface mass density calculation. Simultaneous QCM-D and SE measurements allowed us to extract both wet ($\Gamma^{QCM\text{-}D}$) and dry (Γ^{SE}) surface mass densities and to obtain hydration f_{PBS} of the immobilized FcγRI receptor and IC layers formed during the interaction. For random immobilization of CD64 (Fig. 3A2), the results were similar for all performed experiments, ranging from 100.90 to 117.00 ng cm^{-2} for Γ^{SE}, while the wet surface mass ranged from 515.52 to 569.15 ng cm^{-2}. This resulted in hydration being fairly constant, that is 80%. Differences in both $\Gamma^{QCM\text{-}D}$ and dry Γ^{SE} were observed between SCoV2-S/Nb-Fc ICs. At 90 minutes after the interaction, SCoV2-S/Sb14 (Fig. 3B2) exhibited the highest (92.61 ng cm^{-2}), SCoV2-S/Sb15 (Fig. 3C2) exhibited the lowest (51.13 ng cm^{-2}) and SCoV2-S/Sb68 (Fig. 3D2) exhibited an intermediate Γ^{SE} of 70.05 ng cm^{-2}. Variations of $\Gamma^{QCM\text{-}D}$ differed from Γ^{SE}, the highest being 2460.58 ng cm^{-2} for SCoV2-S/Sb68, followed by 2223.57 ng cm^{-2} for SCoV2-S/Sb14 and the lowest being 2018.27 ng cm^{-2} for the layer of SCoV2-S/Sb15 on CD64. Regarding the SCoV2-S/CR3022 IC layer (Fig. 3E2), Γ^{SE} was higher than any of the ICs formed by Nb-Fc, the closest being to SCoV2-S/Sb14, although $\Gamma^{QCM\text{-}D}$ of SCoV2-S/CR3022 was almost the same as that of SCoV2-S/Sb68. This resulted in SCoV2-S/Sb14 and SCoV2-S/CR3022 being of the same hydration of 95.8-95.9% and SCoV2-S/Sb15 having the hydration value of 97.5%, similar to that of SCoV2-S/Sb68 (f_{PBS} = 97.2%).

Control measurements were conducted with pure Nb-Fcs Sb14 and Sb15, as well as the pure human antibody CR3022 and pure SCoV2-S (Fig. S2). Nb-Fcs and the human antibody did not show any indication of binding to the CD64 receptor, while SCoV2-S exhibited a frequency change of −4.6 Hz, allowing us to calculate the wet surface mass density $\Gamma^{QCM\text{-}D}$ of 181.86 ng cm^{-2}. SE measurements and optical modelling did not measure any dry mass Γ^{SE}, suggesting that pure SCoV2-S, although producing a QCM-D signal, did not effectively bind to the FcγRI receptor, confirming that only the formed ICs were able to interact with CD64.

Competitive analysis of antibody–antigen binding. To investigate SCoV2-S epitopes recognised by Nb-Fcs Sb14, Sb15 and Sb68, as well as their comparison with the human IgG1 antibody CR3022, a competitive analysis was performed with QCM-D (Fig. 4). It allowed for the evaluation of the possible overlaps of antibody paratopes.

Consecutive injection of Sb14, Sb15 and Sb68 on the immobilized SCoV2-S suggested that Sb14 pre-binding prevented subsequent Sb15 binding, as no interaction of Sb15 with SCoV2-S was observed upon injection after the Sb14/SCoV2-S interaction, which resulted in a ΔF of −8.5 Hz. Further injection of Sb68 resulted in a binding event (ΔF = −8.9 Hz), indicating that Sb68 likely recognised a different or spatially distinct binding region from Sb14 and Sb15. To investigate whether these Nb-Fcs showed competitive binding behaviour with CR3022, it was further injected into a QCM-D measurement chamber, and this did not result in any interaction (Fig. 4A). To differentiate the epitopes, further analysis was done (Fig. 4B) on a regenerated SCoV2-S surface. The CR3022/SCoV2-S interaction resulted in a ΔF of −4.3 Hz after washing with PBS. Upon later injection of Sb68 a slight increase by 0.7 Hz of the ΔF curve was observed, consistent with partial dissociation or reorganization. To take a closer look at this behaviour, the interaction was repeated with a reverse order (Fig. 4C). Sb68 was introduced on a clean SCoV2-S surface (ΔF = −4.8 Hz), and CR3022 was injected after. A slight (3 times smaller than CR3022 binding to a clean SCoV2-S surface) ΔF decrease by 1.5 Hz was observed, indicating binding to the SCoV2-S surface. Altogether, these results indicate reduced mutual binding accessibility consistent with overlapping or sterically interfering binding regions, as Fig. 4B and C together depict Sb68 taking the place of CR3022 and CR3022 taking the place of Sb68. The differences in ΔF were different for Sb68 and CR3022 as the molecular weight of Sb68 is smaller than that of CR3022.

Because these sequential-binding experiments were performed using surface-immobilized SCoV2-S and Nb-Fc constructs, the observed responses may reflect epitope overlap as well as steric hindrance, molecule orientation or avidity.

These results are in agreement with already published Sb14, Sb15, Sb68 and CR3022 epitope mapping data; Ahmad *et al.* reported high-resolution structures of Sb14-RBD-Sb68 complexes and showed that Sb14 binds within the ACE2-facing region of the RBD, while Sb68 binds a spatially distinct, peripheral cryptic epitope.[40] The same study showed that the Sb68 binding site is similar to that recognized by CR3022, supporting the observed non-additive binding of Sb68 after CR3022 in our QCM-D experiments.

In addition, Walter *et al.* demonstrated that Sb15 and Sb68 can bind the SARS-CoV-2 spike protein simultaneously.[41] Their

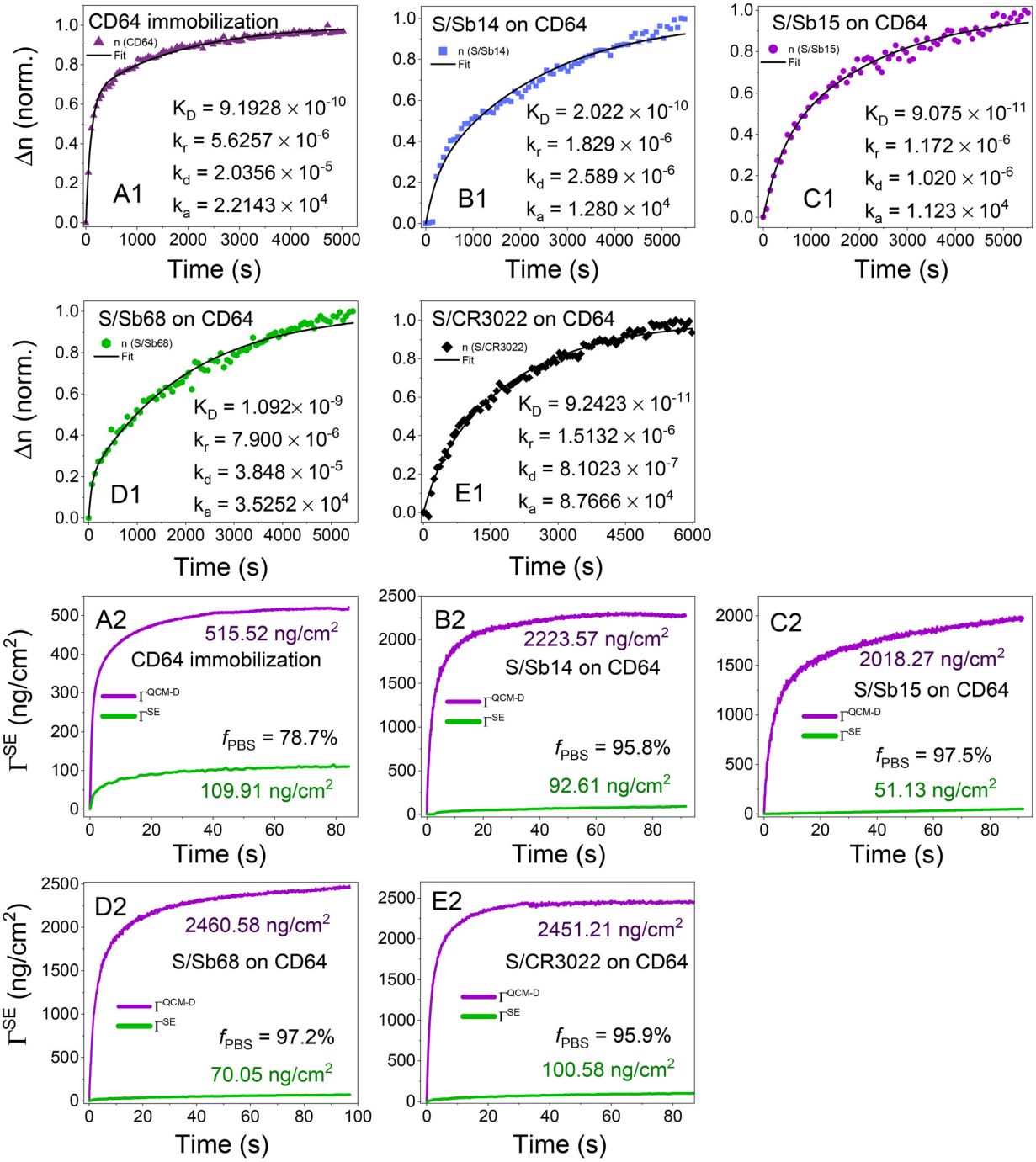


Fig. 3 Analytical signal Δn evolution in time for immobilization of CD64 (A1) and its interactions with ICs: SCoV2-S/Sb14 (B1), SCoV2-S/Sb15 (C1) and SCoV2-S/Sb68 (D1) and SCoV2-S/CR3022 (E1). Kinetic constants – dissociation equilibrium constant K_D, rearrangement (k_r), dissociation (k_d) and association (k_a) rate constants – are displayed in the graphs. The solid line represents a two-step binding kinetic model fit; Wet (Γ^{QCM-D}, violet) and dry (Γ^{SE}, green) surface mass densities for immobilization of CD64 (A2) and its interaction with ICs: SCoV2-S/Sb14 (B2), SCoV2-S/Sb15 (C2), SCoV2-S/Sb68 (D2), and SCoV2-S/CR3022 (E2). f_{PBS} values show calculated hydration. S – SCoV2-S.

cryo-EM analysis placed Sb15 at the ACE2-binding interface and Sb68 at a distinct cryptic epitope on the lateral region of the RBD. This finding supports the interpretation that Sb15 and Sb68 recognize distinct binding regions. Therefore, both Sb14 and Sb15 bind to the broad ACE2-facing region, while Sb68 occupies a separate cryptic region.

In Table 2 we provide quantitative modelling of the competitive QCM-D and SE data to support the observed binding patterns.

In Table 2 are displayed the modelled results of QCM-D and SE data. For the interaction of Sb15 (No. 2) after injection of Sb14 (No. 1), no change in signal was observed, resulting in no

 This journal is © The Royal Society of Chemistry 2026

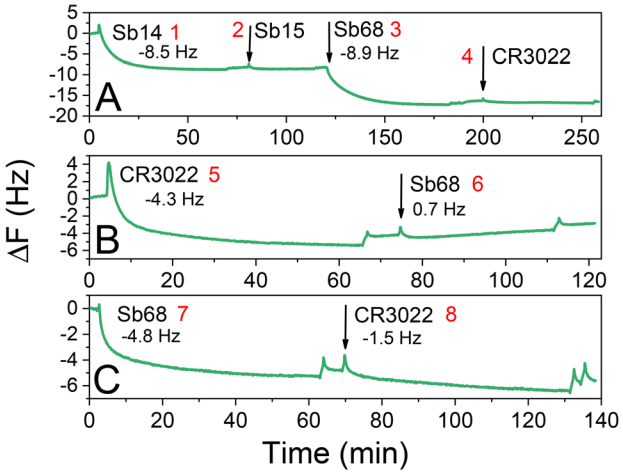


Fig. 4 ΔF change in time of competitive analysis for Sb14, Sb15, Sb68 and CR3022 during the interaction with SCoV2-S. The ΔF curves show that: (A) Sb14 and Sb15 sequential injection results in non-additive binding, sequential injection of Sb68 results in binding, suggesting a different binding site to SCoV2-S than Sb14 and Sb15, while CR3022 binds to one of the epitopes of other Nb-Fcs; (B) Sb68 interaction resulted in a slight surface mass decrease of the formed CR3022 layer, indicating epitope overlap as Sb68 expels CR3022; (C) CR3022 interaction with SCoV2-S after Sb68 resulted in a lower ΔF compared to the injection on a clean SCoV2-S surface, revealing epitope overlap between CR3022 and Sb68. Numbers in red correlate with interaction no. listed in Table 2.

thickness and surface mass densities Γ^{SE} and Γ^{QCM-D}. The same applies for CR3022 injection (No. 4) after the subsequent injection of Sb14, Sb15 and Sb68. During interaction No. 6, when Sb68 was injected after the CR3022 interaction with SCoV-2S a negative change of the surface mass density is observed, which is consistent with a protein of a lower molecular weight (Sb68) competing with that of a higher molecular weight (CR3022). Real-time curves of Γ^{SE} and Γ^{QCM-D} change in time are displayed in the SI (Fig. S3).

Summary of antibody–antigen and IC–FcγRI interactions. To compare antibody–antigen and IC–FcγRI interactions, we made their visualizations (Fig. 5) based on our experimental results. The summary of the main parameters of the evaluation of interaction kinetics, surface mass density and formed layers' properties is shown in Table 2.

On summarizing antibody affinity characterization and formed IC interactions with FcγRI, we found several differences (Fig. 5 and Table 2). The calculated K_D values showed very high antibody affinity to SCoV2-S, although one of the Nb-Fc, Sb14, had higher affinity compared to others. The free Gibbs energy for association was also the highest for Sb14 and SCoV2-S complex formation (ΔG_{bind} = −59.9 kJ mol^{-1}, Fig. 5). Moreover, Sb14 formed the IC of the largest size. However, its IC did not have the highest affinity to FcγRI, although it bound to FcγRI very strongly compared to others. Comparing the amount of IC bound (dry mass, ΓSE) to FcγRI, the Γ^{SE} of SCoV2-S/Sb14 was the highest among ICs of Nb-Fc. Taken together, the Sb14 antibody acted differently compared to other Nb-Fcs. Interestingly, we observed the differences between Sb14 and Sb15 that have the same or very adjacent epitopes. In addition, for the interaction of IC with FcγRI, the $\Delta D/\Delta F$ curve follows a non-linear path, indicating slight conformational changes during molecular interactions in all cases (Fig. S1, 5th harmonics). All Nb-Fcs had high affinity to SCoV2-S and interacted with FcγRIs in a comparable way to the CR3022 antibody, although the IC formed by CR3022 showed the highest ΔD during FcγRI and IC interactions. On the other hand, the CR3022 antibody is relatively larger compared to Nb-Fcs and tends to have a higher ΔD as a result of more tightly coupled PBS. Due to these differences, we conducted a further functional analysis of ICs focusing on the differences of Nb-Fcs and using CR3022 as a control conventional antibody. Our goal was to relate their characterization to innate immune cell activation. These cells are responsible for removing the formed ICs in the body. The innate immune cells phagocytose the ICs *via* FcRs on their surface. After this process cell activation can be induced (Table 3).

Innate immune response to ICs formed by SCoV2-S and Nb-Fcs. As an innate immune cell model, we used macrophages differentiated from the THP-1 monocytic cell line. Firstly, we evaluated the uptake of SCoV2-S and their ICs formed by Nb-Fcs. All of them were taken up by macrophages; however, the ICs were phagocytosed to a higher extent (Fig. 6). The use of the actin polymerization inhibitor cytochalasin D revealed that ICs are phagocytosed, but SCoV2-S enters the cells likely by a passive endocytosis process (Fig. 6B), such as pinocytosis as described with small molecular mass protein particles soluble amyloid beta oligomers.[42] In addition, cytochalasin D did not

Table 2 Quantitative SE/QCM-D parameters for sequential binding experiments of Sb14, Sb15, Sb68, and CR3022 on immobilized SCoV2-S. Thickness, dry surface mass (Γ^{SE}) and wet surface mass (Γ^{QCM-D}) values were derived only where the change in signal was observed. The negative Γ^{QCM-D} value indicates the decrease in surface mass

No.	Interaction	Thickness (SE), nm	Γ^{SE}, ng cm^{-2}	Γ^{QCM-D}, ng cm^{-2}
1	Sb14 on S	5.58 ± 0.782	68.55	147.77
2	Sb15 on Sb14/S	—	—	—
3	Sb68 on Sb15/Sb14/S	4.16 ± 0.832	26.84	157.75
4	CR3022 on Sb68/Sb15/Sb14/S	—	—	—
5	CR3022 on S	8.76 ± 0.917	97.07	1083.73
6	Sb68 (together with CR3022) on S	8.10 ± 2.065	2.26	−151.82
7	Sb68 on S	3.60 ± 0.343	19.06	110.15
8	CR3022 on Sb68/S	4.27 ± 0.489	1.88	21.11

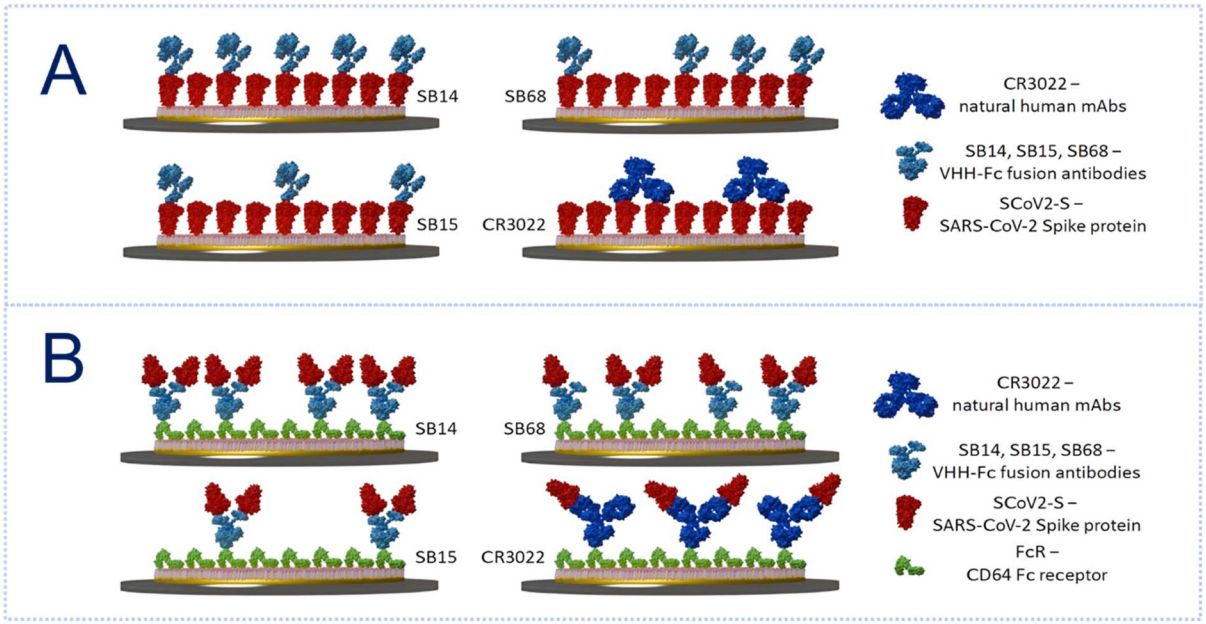


Fig. 5 Schematic representation of Nb-Fc affinity characterization and the formed immune complex (IC) interaction with covalently immobilized FcγRI (CD64), including comparison with the natural human IgG1 antibody (CR3022). (A) Antibody affinity interaction with SCoV2-S. (B) FcγRIs interaction with ICs formed by SCoV2-S and different Nbs Sb14, Sb15, Sb68, and the natural human antibody CR3022.

Table 3 Antibody and IC layers, affinity constants (K_D), surface mass density (Γ^{SE}, $\Gamma^{QCM\text{-}D}$), hydration (f_{PBS}), Gibbs free energy change (ΔG_A) of antibodies during the interaction with SCoV2-S, ΔD change over time for IC/FcR (CD64) complex formation

Layer	Layer, nm	K_D, M	Γ^{SE}, ng cm^{-2}	$\Gamma^{QCM\text{-}D}$, ng cm^{-2}	f_{PBS}, %	ΔD (7th harmonic)	ΔG_A, kJ mol^{-1}
Sb14 on SCoV2-S	4.32	2.10×10^{-11}	53.14	—	—	—	−59.9
Sb15 on SCoV2-S	4.05	3.68×10^{-10}	45.1	—	—	—	−52.9
Sb68 on SCoV2-S	2.65	2.99×10^{-10}	39.06	—	—	—	−53.5
CR3022 on SCoV2-S	9.09	4.07×10^{-10}	30.63	—	—	—	−52.7
SCoV2-S/Sb14 on CD64	21.90	2.02×10^{-10}	92.61	2223.57	95.8	1.5	−54.4
SCoV2-S/Sb15 on CD64	18.05	9.08×10^{-11}	51.13	2018.27	97.5	1.2	−56.4
SCoV2-S/Sb68 on CD64	20.69	1.09×10^{-9}	70.05	2460.58	97.2	2.0	−50.3
SCoV2-S/CR3022 on CD64	30.00	9.24×10^{-11}	100.58	2451.21	95.9	3.0	−56.3

inhibit ICs' entry to the cells completely but to the level of SCoV2-S treatment (Fig. 6B). On comparing the phagocytosis of ICs formed by Nb-Fcs with CR3022, we have not observed any differences. These data show that ICs formed by Nb-Fcs and SCoV2-S are phagocytosed, demonstrating Nb-Fc's similarity to natural human antibodies.

To evaluate the phagocytosis of SCoV2-S ICs at the single-cell level, we applied flow cytometry analysis. The results were consistent with the microscopy findings: low SCoV2-S-Green pHrodo fluorescence was detected in most cells. Only a small fraction of cells was SCoV2-S-positive after treatment with ICs, ranging from 4% to 7% of SCoV2-S-positive cells. Also, no SCoV2-S-positive cells were detected after treatment with only the SCoV2-S antigen (Fig. S5). This shows that only a small population of cells have taken up ICs.

To show FcR-dependent SCoV2-S IC phagocytosis, we applied the antibody-based Fc-blocking solution that blocks FcγRI, FcγRII, and FcγRIII. The results demonstrated that SCoV2-S ICs are specifically phagocytosed *via* FcRs (Fig. 7 and Fig. S6). However, the FcR blocker did not completely reduce the uptake of SCoV2-S ICs, possibly because the FcR blockade is fundamentally a reversible process as it relies on non-covalent, competitive binding. The blocking solution saturates the receptors through dynamic equilibrium, meaning that the blocker molecules continuously bind and dissociate from the receptors. Nb-Fcs were also phagocytosed to a similar extent to CR3022 IC, further supporting their Fc-mediated effector functions and their similarity to conventional antibodies.

Next, we investigated macrophage response to ICs formed by Nb-Fcs, evaluating inflammatory signals. First, we evaluated SCoV2-S cytotoxicity by measuring LDH release. SCoV2-S and their ICs did not affect the cell viability (Fig. 8A). SCoV2-S also did not induce inflammatory cytokine (IL-1β, TNF-α) secretion (Fig. 8B and C). These data show that although the ICs are phagocytosed by macrophages, they do not induce an inflammatory response.

Furthermore, we analysed whether SCoV2-S and their ICs induce cellular molecules related to antigen presentation on

 This journal is © The Royal Society of Chemistry 2026

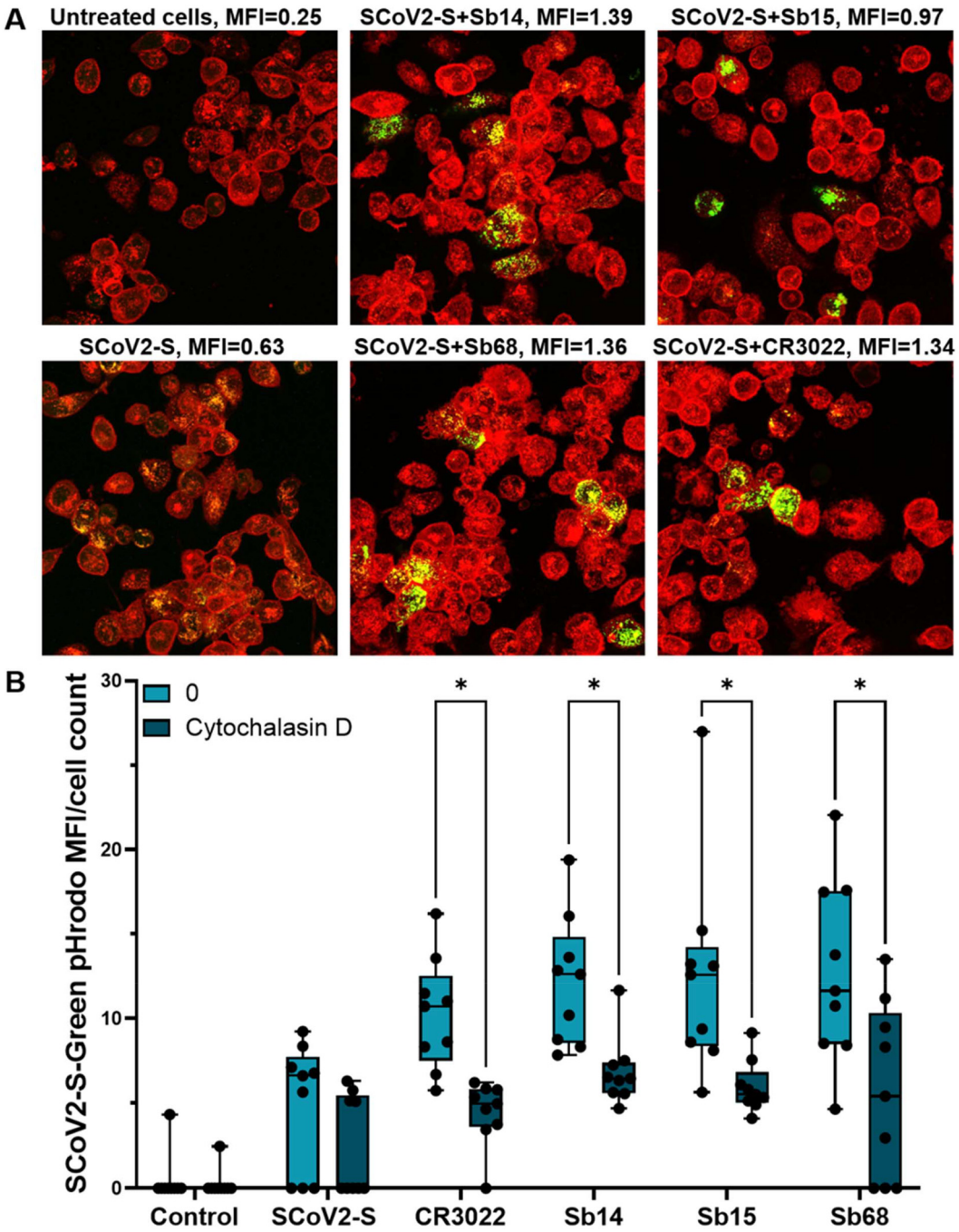


Fig. 6 Phagocytosis analysis of SCoV2-S and their ICs in THP-1 macrophages. Cells were treated with SCoV2-S or ICs for 3 h, and live cells were used for microscopy analysis. SCoV2-S labelled with Green pHrodo dye was used for the assays. It fluoresces at low pH – in lysosomes. Cell membranes were labelled with the deep red cell membrane stain 30 min before microscopy analysis. Live cells were imaged using Live Cell Imaging Solution. (A) Representative *Z*-projection of 3D images made by a confocal microscope. Orthogonal views are shown in Fig. S4. Composite images are shown, colours represent red – cell membrane stain, green – SCoV2-S signal, yellow – the overlay. An average MFI value of 6 3D images is shown. (B) Quantification of the SCoV2-S signal per cell of wide-field microscopy photos. Representative images are shown in Fig. S4. One dot in a bar graph represents one photo (n = 10 technical repeats), N = 1. Unpaired Student t-test was used to test for significant differences, *$p < 0.05$. MFI – mean fluorescence intensity.

the macrophage surface. These molecules are often co-expressed during antigen presentation, and their co-stimulatory signals mediate appropriate contact between T cells and antigen-presenting cells and facilitate signal transduction.[43] We selected CD86 and CD83. CD86 expression can also indicate a pro-inflammatory response.[44,45] CD83 expression is very dynamic, and it serves as a regulatory molecule in antigen presentation.[46] CD83 expression is also related to the resolu-

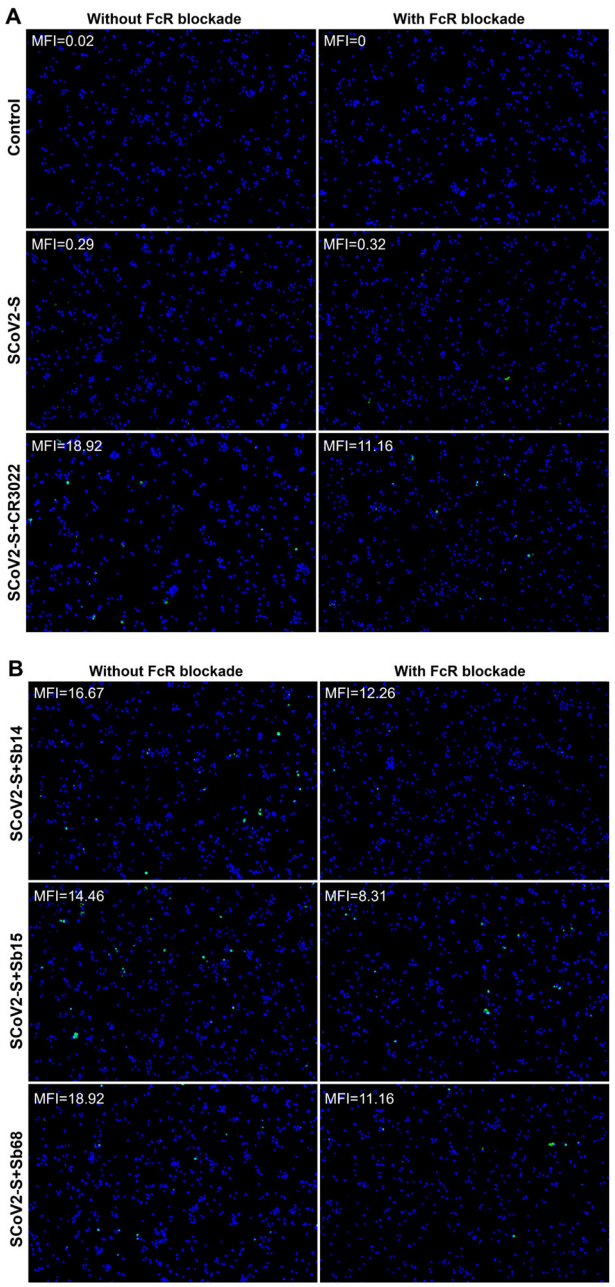


Fig. 7 SCoV2-S and their ICs phagocytosis blocking by FcR inhibitors in THP-1 macrophages. Cells were treated with SCoV2-S or ICs for 3 h, and live cells were used for microscopy analysis. SCoV2-S, labelled with the Green pHrodo dye, was used for the assays. It fluoresces at low pH – in lysosomes. Nuclei were stained with Hoechst 33342 (blue) 30 min before microscopy analysis and used for cell number quantification. An antibody-based FcR-blocking strategy was used to determine the mechanisms of ICs' phagocytosis. Images of SCoV2-S with pHrodo Green (green) and nuclei (blue) signals were acquired using a wide-field microscope (N = 1). Large images of 8 × 8 fields (2673.23 × 2673.23 microns) were captured for each condition (Fig. S6). Cropped composite images are shown, colours represent green – SCoV2-S signal, blue – nucleus. The treatment conditions: (A) control, SCoV2-S, SCoV2-S+CR3022; (B) SCoV2-S+Sb14, SCoV2-S+Sb15, SCoV2-S+Sb68. The values of mean fluorescence intensity (MFI) per cell for large images are shown in the cropped images.

tion of inflammation after cell encounter with various mediators.[47] We found that neither SCoV2-S nor ICs influenced cell surface exposure of CD86, but a different impact was on the cell surface expression of CD83 (Fig. 8D, E and Fig. S7A, B). ICs formed by Sb15 and Sb68 significantly increased the cell surface exposure of CD83 (Fig. 8D). Interestingly, IC formed by the highest affinity Nb-Fc (Sb14) did not affect the cellular expression of CD83. This IC was also of the highest relative size and bound to FcγRI to the highest extent (according to the surface mass density, Table 2) compared to others. This result shows that CD83 is more likely to be induced by relatively smaller ICs. As CD83 expression is associated with the resolution of inflammation, we tested whether it is not related to M1/M2 macrophage polarisation. ICs of Nb-Fcs or CR3022 did not induce cell-surface expression of the M1 marker CD86 (Fig. 8E), which can also indicate the presence of M2 subpopulations. Moreover, we did not detect other inflammatory markers, including IL-β and TNF-α secretion (Fig. 8B and C). We also did not detect any secretion of the anti-inflammatory cytokine IL-10. The detected IL-10 concentration in the cell culture supernatant was below the assay's detection limit. Therefore, we hypothesise that CD83 expression is not directly associated with M1/M2 macrophage polarisation but is instead more likely linked to a regulatory macrophage phenotype.

Finally, to evaluate macrophage response to ICs formed by Nb-Fc we examined the chemokine CCL2/CCR2 and CCL5/CCR5 axes. These molecules transduce communication signals between the cells.[48] They are secreted during infection or as cell communication molecules under physiological conditions, or in response to damage. Macrophages utilise these molecules to convey signals to other immune cells.[49] They secrete these molecules not necessarily during inflammation. Also, as macrophages express the relevant chemokine receptors (CCR2 and CCR5), they can secrete CCL2 and CCL5 to other macrophage cells and have autocrine and paracrine signalling effects at the same time.[50] We did not find SCoV2-S or their ICs effect on CCL5 secretion (Fig. 8F) and CCR5 cell surface expression (Fig. 8G and Fig. S7D). Also, SCoV2-S or their ICs did not induce CCL2 secretion compared to cells treated with the antibody control (Fig. 8H). We observed that ICs formed by Sb15 and Sb68 induced higher cell surface expression of CCR2 (Fig. 8H and Fig. S7C); however, it was not statistically significant due to a high data variation (Fig. 8I). Nevertheless, only these ICs had an effect on CCR2 expression, as well as on CD83.

Comparing macrophage activation by ICs formed by Nb-Fcs with CR3022, we have observed the differences related to the formed IC structure. ICs formed by CR3022 had the same effect on macrophage response as ICs formed by Sb14 (Fig. 7). This emphasises the similarity of Nb-Fcs to conventional IgG1 antibodies and the impact of structural properties on IC-mediated phagocytic immune cell activation.

Discussion

Fc-fusion Nbs are highly applicable due to their ease and stability of immobilization, as well as enhanced avidity. In surface

 This journal is © The Royal Society of Chemistry 2026

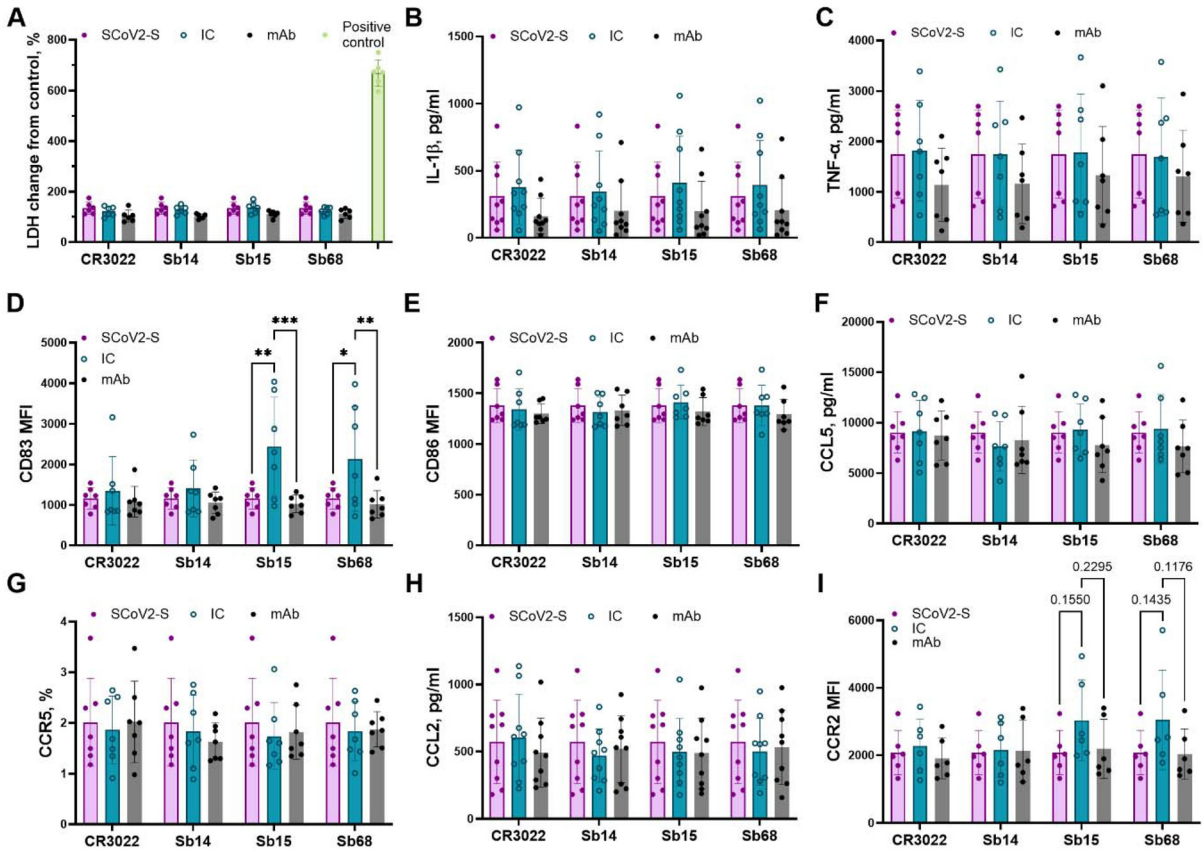


Fig. 8 THP-1 macrophage activation by SCoV2-S and their ICs. Cells were treated with SCoV2-S or ICs for 24 h, cell culture supernatants and whole cells were collected for the following assays. (A) LDH release showing cell metabolic activity. Triton X-100 was used to lyse the cells as a positive control. Secretion of inflammatory cytokines: (B) IL-β, (C) TNF-α, determined by ELISA. Surface expression of co-stimulatory molecules related to antigen presentation: (D) CD86, (E) CD83, determined by flow cytometry. Chemokine secretion: (F) CCL5, (H) CCL2, determined by ELISA. Cell surface expression of chemokine receptors: (G) CCR5, (I) CCR2, determined by flow cytometry. Data are shown by bar graphs with individual data points showing independent cell culture preparations (N = 6–8). To test for statistically significant differences two-way ANOVA followed Tukey's multiple comparisons test was performed, *p < 0.05, **p < 0.01, ***p < 0.001. mAb – monoclonal antibody control refers to all Nb-Fcs (Sb14, Sb15, Sb68) and CR3022, MFI – mean fluorescence intensity.

plasmon resonance analysis, Nb-Fc fusions such as VHH-72-Fc were covalently immobilized on PEG-COOH-modified gold chips, yielding tighter RBD binding ($K_D \approx 1.5 \times 10^{-9}$ M; $k_{off} \approx 1.8 \times 10^{-4}$ s^{-1}) than the monovalent Nb.[51] Another benefit of engineered Nbs, such as His-tagged or Fc-fusion, is the aid in purification or immobilization *via* protein G/A, as well as the ability to achieve reversible immobilization Ni-NTA sensors.[52–56] These findings support Nb-Fc and related multivalent Nb construct usage, given their potentially enhanced binding strength and broad epitope coverage in the case of IC formation.

In the present work, we used Nbs coupled with the antibody Fc fragment (Nb-Fc) and analysed their functional activity, including the interaction with FcRs as their application as a medical tool, immune modulation and antigen removal. The latter properties have not been investigated enough. For this study, we selected FcγRI, also known as CD64, which is highly expressed on macrophages and plays an activation role in cell signalling pathways.[14] It is involved in the phagocytosis process, oxidative burst, production of inflammatory molecules, *etc*. We randomly immobilized SCoV2-S and FcγRI on a gold-covered sensor disc. Following immobilization, we measured the interaction kinetics of real-time Nb-Fc/SCoV2-S immune complex formation by TIRE that allowed us to calculate kinetic parameters K_D, ΔG_A, and dry surface mass density (Γ^{SE}). We found that all investigated Nb-Fcs had high affinity to SCoV2-S. We were also able to obtain differences between the formation of these ICs. One of our ICs formed a relatively larger complex compared to others. This Nb-Fc Sb14 had the highest affinity to SCoV2-S. We also evaluated the FcγRI affinity interaction with ICs formed by SCoV2-S and different Nb-Fcs by two methods simultaneously, QCM-D and SE, which allowed us to obtain kinetic parameters, including K_D, dissipation parameter ΔD, and both dry (Γ^{SE}) and wet (including buffer, $\Gamma^{QCM\text{-}D}$) surface mass densities for all formed protein monolayers. ΔD conveyed about the viscoelastic properties of the formed layer and possible conformational changes that occur during protein–protein interactions. ΔD values showed

that the IC–FcγRI interaction is a very dynamic process, and it was similar for all ICs formed by different Nb-Fcs. K_D values differed for the ICs, although all of them exhibited high affinity to FcγRI. The highest K_D of interaction with FcγRI was of the IC formed by Sb15, while K_D for IC of the highest affinity Nb-Fc Sb14 was intermediate. This shows that antibody affinity to the antigen does not describe its IC interaction with FcγRI. The $\Gamma^{QCM\text{-}D}$ value allowed us to calculate the hydration of the formed IC/FcγRI layers. It was similar between different ICs; nevertheless, the hydration of the IC formed by Sb14 was the lowest compared to other Nb-Fcs. On comparing the dry surface mass density (Γ^{SE}) of the formed IC/FcγRI layers, we found similar results to those for IC/FcγRI layers. The relatively largest IC formed by Sb14 also resulted in the highest dry surface mass density of the formed IC/FcγRI layer. Overall, Sb14 distinguished itself in all characteristics.

Optical methods, such as Surface Plasmon Resonance (SPR), has been applied to study IgG interactions with various FcRs, but the experiments usually do not explore pre-formed IC interactions with the receptors, as it was well-summarized by Forest-Nault *et al.*[26] When precise kinetic measurements are required, SE with a two-step binding model proves to be a more suitable optical biosensing technique than SPR.[38] In cells, the receptor CD64 can be occupied by monomeric IgG antibodies present in the serum, but that does not result in receptor activation.[57] The assay geometry has been reported to have a minor impact on IgG interaction kinetics with FcRs, while pre-formed antigen–IgG immune complexes produced improved apparent binding to most FcRs and improved IgG1–FcR binding by >100 fold in some cases, proving ICs as the relevant ligands for FcRs.[58]

We also compared our results on SCoV2-S/Nb-Fc and the IC of Nb-Fc/FcγRI interactions with those of the natural human IgG1 antibody CR3022. We found that Nb-Fc interacted in a comparable manner to CR3022; however, CR3022 is almost twice as large as Nb-Fc; therefore, it showed different parameters related to the surface mass density. Also, the ΔD value was higher due to its higher molar mass and amount of coupled PBS. CR3022 to SCoV2-S K_D was of the same order as for Sb15 and Sb68, while the formed IC K_D to FcγRI was almost equal to the IC formed with Sb15. These data revealed that Nb-Fcs promote antigen clearance and that the resulting ICs interact with cell surface FcRs, leading to phagocytosis and cell activation, while these effects depend on the antibody and IC properties. It has been shown that the IC architecture, particularly size, valency, and flexibility, directly tune FcR engagement, with larger ICs generally having more sufficient binding to FcRs, although this is more relevant during experiments that explore cell signaling.[57,59,60] Our QCM-D/SE results have shown that the Nb-Fc IC affinity is comparable to the IC formed by the conventional monoclonal antibody CR3022 despite the difference in size when interacting with the immobilized CD64, but a tendency could be observed when comparing Nbs; the biggest IC formed by Nb Sb14 resulted in the highest Γ^{SE} despite sharing the same epitope and being of lower K_D than the smaller IC SCoV2-S/Sb15. Precise evaluation of IC parameters using QCM-D and SE allows us to determine which parameters (size, epitope or affinity) are more responsible for certain cellular functions.

To evaluate Nb-Fc functional activity in the biological system, we investigated the interaction of ICs formed by different Nb-Fc with phagocytic innate immune cells, macrophages. We used an *in vitro* THP-1 cell-based macrophage cell culture model. We measured the macrophage response to these ICs by evaluating IC phagocytosis, further inducing an inflammatory response and the expression of molecules related to antigen presentation, as well as the chemokine axis CCL2/CCR2 and CCL5/CCR5, which indicate further communication between immune cells. We found that all ICs were phagocytosed by macrophages, showing the primary IC interaction with FcR on the cell surface. However, we did not detect the secretion of inflammatory cytokines. This demonstrates that ICs formed by the viral protein antigen SCoV2-S do not induce an inflammatory response in macrophages. Although some studies show that SCoV2-S itself can mediate pro-inflammatory signals in these cells.[61,62] Macrophages just remove these ICs from their surroundings. We also did not detect cell surface expression of the co-stimulatory molecule CD86, which is involved in antigen presentation and inflammatory responses. However, we found that ICs can induce cell surface expression of another co-stimulatory molecule, CD83, which is associated with the resolution of inflammation. Interestingly, not all ICs had this effect, only ICs formed by Sb15 and Sb68. Comparing these ICs with ICs formed by the highest affinity Nb-Fc Sb14, Sb14 formed relatively the largest ICs that covered the FcR surface with the highest mass density. These data show that CD83 cell surface expression can be induced by relatively smaller and less dense ICs, considering the antigen properties, as we used only the viral protein SCoV2-S. Our previous results show that relatively large ICs formed by very high-affinity antibodies have a different effect on macrophage activation than the others.[34] In this case, the IC enhanced the viral antigen-induced inflammatory response. On the other hand, in our current research the viral antigen itself did not have any effect on inflammatory signals; thus, this could lead to different outcomes. Based on our combined biophysical and cellular data, we propose that the structural properties of immune complexes (ICs), including their size, density, and epitope organisation, influence FcγRI clustering and downstream signalling, thereby affecting antigen presentation. Furthermore, highly dense or large ICs (Sb14) may promote a distinct pattern of receptor organisation compared with smaller ICs, leading to different signalling outcomes. However, the relationship between the physicochemical properties of ICs and CD83 induction is based on correlative analyses and therefore requires further mechanistic investigation to establish causality.

CD83 is constitutively expressed in macrophages, but its cell surface expression is a highly dynamic process. Normally, soluble CD83 or CD83 expressed on the cell surface have their functional activity.[63] In macrophages, this molecule can determine the early response to specific mediators.[64] In contrast to CD86, having pro-inflammatory properties, CD83 has an

 This journal is © The Royal Society of Chemistry 2026

inhibitory effect on macrophage polarization to the inflammatory state, called M1.[65] CD83 removal can hinder the resolution of inflammation, leading to chronic inflammation, cell apoptosis, and fibrosis.[47] This function of CD83 is quite new and our data show for the first time the relationship of CD83 cell surface expression with IC properties. Also, for the first time, we made a comprehensive analysis of Nb-Fc characterization, their formed IC interaction with FcRs and *in vitro* analysis of macrophage response to ICs of different properties. These data could be relevant for the applications of Nb-Fc in medicine, as a tool in diagnostic systems, or for scientific investigations.

Despite the insights gained from this study, several limitations should be acknowledged. First, all functional experiments were performed using THP 1-derived macrophages, which represent a simplified model of innate immune responses and do not fully capture the heterogeneity and complexity of primary human immune cells. Second, the study is limited to *in vitro* conditions and therefore does not account for physiological factors such as systemic immune regulation, Fc receptor diversity, or tissue-specific effects that may influence Nb Fc activity *in vivo*. Future studies employing human macrophages, peripheral blood mononuclear cells, and other innate immune cells, including NK cell models and neutrophils, are required to evaluate the Fc-engineered Nb-Fc functionality across immune effector mechanisms such as antibody-dependent cellular cytotoxicity (ADCC). In addition, *in vivo* validation using appropriate animal models, such as human FcγR transgenic mice, will be essential to determine the therapeutic potential, safety, and functional efficacy of Nb Fc constructs in complex biological environments.

Conclusions

In this study, we compared Nb-Fc functional properties with the natural human IgG1 antibody CR3022. Our results demonstrated that Nb-Fc behaves in a similar way to a natural human antibody, considering the affinity interaction with a specific antigen and the formed IC interaction with FcγRI. In addition, our comprehensive analysis enabled us to differentiate Nb-Fcs according to their properties related to the measured macrophage activation. We found that one of our ICs, formed by the highest affinity Nb-Fc, induced the cell surface expression of the CD83 molecule related to the resolution of inflammation. Our results underscored that antibody affinity is a key factor in determining the functional activity of the formed IC. Here, we performed a comprehensive characterization of Nbs coupled with the Fc fragment and showed their similarities to a conventional human antibody, including IC formation with a specific antigen and IC affinity interaction with FcRs. While these findings provide important mechanistic insights into Nb-Fc functionality, they represent proof-of-concept observations in an *in vitro* model system. Further validation in primary human immune cells and *in vivo* models will be required to fully establish their translational and therapeutic relevance. Our results could be used for further Nb characterization and contribute to the further development of diagnostic tools and medical applications.

Author contributions

Migle Stanciauskaite: investigation; methodology; visualisation; writing and revising – original draft. Asta Lučiūnaitė: conceptualisation; supervision; investigation; methodology; writing and revising – original draft; visualisation. Mantvydas Usvaltas: investigation; visualisation; writing and revising – original draft. Kristina Mašalaitė: investigation; visualisation. Ieva Plikusiene: conceptualisation; supervision; methodology; writing – review & editing; funding acquisition.

Conflicts of interest

The authors declare no competing financial interests or conflicts of interest associated with this research.

Data availability

The data supporting this study are available within the article and its supplementary information (SI). Supplementary information is available. See DOI: https://doi.org/10.1039/d6bm00509h.

Acknowledgements

This research was funded by a grant (no. S-MIP-23-82) from the Research Council of Lithuania.

References

1 M. I. Mustafa and A. Mohammed, Nanobodies: A Game-Changer in Cell-Mediated Immunotherapy for Cancer, *SLAS Discovery*, 2023, **28**, 358–364, DOI: 10.1016/j.slasd.2023.08.008.

2 A. W. Tarr, P. Lafaye, L. Meredith, L. Damier-Piolle, R. A. Urbanowicz, A. Meola, J.-L. Jestin, R. J. P. Brown, J. A. McKeating, F. A. Rey, J. K. Ball and T. Krey, An Alpaca Nanobody Inhibits Hepatitis C Virus Entry And Cell-To-Cell Transmission, *Hepatology*, 2013, **58**, 932–939.

3 P. Safarzadeh Kozani, A. Naseri, S. M. J. Mirarefin, F. Salem, M. Nikbakht, S. Evazi Bakhshi and P. Safarzadeh Kozani, Nanobody-based CAR-T cells for cancer immunotherapy, *Biomark. Res.*, 2022, **10**, 1–18, DOI: 10.1186/s40364-022-00371-7.

4 J. Jeon, C. Cho, S. Kim, H. Kim, H. Lee, S. J. Kim, H. Park, J. H. Yu, S. Lee, K. S. Lee, J. Jung and S. Yang, Blockade of the vaspin–AP-1 axis inhibits arthritis development, *Exp. Mol. Med.*, 2025, **57**, 628–636, DOI: 10.1038/s12276-025-01418-z.

5 R. Van Campenhout, T. W. M. De Groof, P. Kadam, B. R. Kwak, S. Muyldermans, N. Devoogdt and M. Vinken, Nanobody-based pannexin1 channel inhibitors reduce inflammation in acute liver injury, *J. Nanobiotechnol.*, 2023, **21**, 1–20, DOI: 10.1186/s12951-023-02137-1.

6 A. Mahindra, G. Tejeda, M. Rossi, O. Janha, I. Herbert, C. Morris, D. C. Morgan, W. Beattie, A. C. Montezano, B. Hudson, A. B. Tobin, D. Bhella, R. M. Touyz, A. G. Jamieson, G. S. Baillie and C. M. Blair, Peptides derived from the SARS-CoV-2 receptor binding motif bind to ACE2 but do not block ACE2-mediated host cell entry or pro-inflammatory cytokine induction, *PLoS One*, 2021, **16**, e0260283, DOI: 10.1371/JOURNAL.PONE.0260283.

7 Q. Liu, Y. Lu, C. Cai, Y. Huang, L. Zhou, Y. Guan, S. Fu, Y. Lin, H. Yan, Z. Zhang, X. Li, X. Yang, H. Yang, H. Guo, K. Lan, Y. Chen, S. C. Hou and Y. Xiong, A broad neutralizing nanobody against SARS-CoV-2 engineered from an approved drug, *Cell Death Dis.*, 2024, **15**, 458, DOI: 10.1038/s41419-024-06802-7.

8 R. Maeda, J. Fujita, Y. Konishi, Y. Kazuma, H. Yamazaki, I. Anzai, T. Watanabe, K. Yamaguchi, K. Kasai, K. Nagata, Y. Yamaoka, K. Miyakawa, A. Ryo, K. Shirakawa, K. Sato, F. Makino, Y. Matsuura, T. Inoue, A. Imura, K. Namba and A. Takaori-Kondo, A panel of nanobodies recognizing conserved hidden clefts of all SARS-CoV-2 spike variants including Omicron, *Commun. Biol.*, 2022, **5**, 1–16, DOI: 10.1038/s42003-022-03630-3.

9 J. M. Zupancic, M. D. Smith, H. Trzeciakiewicz, M. E. Skinner, S. P. Ferris, E. K. Makowski, M. J. Lucas, N. McArthur, R. S. Kane, H. L. Paulson and P. M. Tessier, Quantitative flow cytometric selection of tau conformational nanobodies specific for pathological aggregates, *Front. Immunol.*, 2023, **14**, 1164080, DOI: 10.3389/FIMMU.2023.1164080.

10 G. Ye, J. Gallant, J. Zheng, C. Massey, K. Shi, W. Tai, A. Odle, M. Vickers, J. Shang, Y. Wan, L. Du, H. Aihara, S. Perlman, A. Lebeau and F. Li, The development of nanosota-1 as anti-sars-cov-2 nanobody drug candidates, *eLife*, 2021, **10**, e64815, DOI: 10.7554/ELIFE.64815.

11 G. Ruiz-Vega, M. Soler, M. C. Estevez, P. Ramirez-Priego, M. D. Pazos, M. A. Noriega, Y. Margolles, C. Francés-Gómez, R. Geller, G. Matusali, F. Colavita, A. di Caro, J. M. Casasnovas, L. A. Fernández and L. M. Lechuga, Rapid and direct quantification of the SARS-CoV-2 virus with an ultrasensitive nanobody-based photonic nanosensor, *Sens. Diagn.*, 2022, **1**, 983–993, DOI: 10.1039/D2SD00082B.

12 N. Meng, X. Cheng, M. Sun, Y. Zhang, X. Sun, X. Liu and J. Chen, Screening, Expression and Identification of Nanobody Against Monkeypox Virus A35R, *Int. J. Nanomed.*, 2023, **18**, 7173–7181, DOI: 10.2147/IJN.S431619.

13 R. Jefferis, J. Lund and J. D. Pound, IgG-Fc-mediated effector functions: molecular definition of interaction sites for effector ligands and the role of glycosylation, *Immunol. Rev.*, 1998, **163**, 59–76, DOI: 10.1111/J.1600-065X.1998.TB01188.X.

14 S. Ben Mkaddem, M. Benhamou and R. C. Monteiro, Understanding Fc Receptor Involvement in Inflammatory Diseases: From Mechanisms to New Therapeutic Tools, *Front. Immunol.*, 2019, **10**, 811, DOI: 10.3389/FIMMU.2019.00811.

15 Nomenclature of the Fc receptors, IUIS subcommittee on nomenclature – PubMed, https://pubmed.ncbi.nlm.nih.gov/2805222/(accessed November 12, 2025).

16 D. Mancardi and M. Daëron, Fc Receptors in Immune Responses, *Ref. Mod. Biomed. Sci.*, 2014, DOI: 10.1016/B978-0-12-801238-3.00119-7.

17 S. Frampton, R. Smith, L. Ferson, J. Gibson, E. J. Hollox, M. S. Cragg and J. C. Strefford, Fc gamma receptors: Their evolution, genomic architecture, genetic variation, and impact on human disease, *Immunol. Rev.*, 2024, **328**, 65–97, DOI: 10.1111/IMR.13401.

18 Y. Li, H. Shen, R. Zhang, C. Ji, Y. Wang, C. Su and J. Xiao, Immunoglobulin M perception by FcμR, *Nature*, 2023, **615**, 907–912, DOI: 10.1038/s41586-023-05835-w.

19 S. Crescioli, S. Jatiani and L. Moise, With great power, comes great responsibility: the importance of broadly measuring Fc-mediated effector function early in the antibody development process, *mAbs*, 2025, **17**, 2453515, DOI: 10.1080/19420862.2025.2453515.

20 N. Nath, B. Godat, R. Flemming and M. Urh, Deciphering the Interaction between Neonatal Fc Receptor and Antibodies Using a Homogeneous Bioluminescent Immunoassay, *J. Immunol.*, 2021, **207**, 1211–1221, DOI: 10.4049/JIMMUNOL.2100181.

21 H. Fan, M. Chen, R. Li, Y. Chen, S. Zeng, W. Hu, G. L. Liu, C. Sun and L. Huang, A miniaturized microfluidic nanoplasmonic sensor with cavity reflection enhancement for ultrasensitive molecular interaction analysis, *Chem. Eng. J.*, 2024, **499**, 155896, DOI: 10.1016/J.CEJ.2024.155896.

22 S. Yanaka, H. Watanabe, R. Yogo, M. Kongsema, S. Kondo, H. Yagi, T. Uchihashi and K. Kato, Quantitative Analysis of Therapeutic Antibody Interactions with Fcγ Receptors Using High-Speed Atomic Force Microscopy, *Biol. Pharm. Bull.*, 2024, **47**, 334–338, DOI: 10.1248/BPB.B23-00751.

23 J. D. Mohr, M. Ramezani, D. Holowka and B. A. Baird, Micropatterned Ligand Arrays to Investigate Spatial Regulation of Cellular Signaling Initiated by Clustered Fc Receptors, *Methods Mol. Biol.*, 2022, **2421**, 1–19, DOI: 10.1007/978-1-0716-1944-5_1.

24 N. Nath, B. Godat, R. Flemming and M. Urh, A homogeneous bioluminescent immunoassay for parallel characterization of binding between a panel of antibodies and a family of Fcγ receptors, *Sci. Rep.*, 2022, **12**, 1–14, DOI: 10.1038/s41598-022-15887-z.

25 J. Dorion-Thibaudeau, G. St-Laurent, C. Raymond, G. De Crescenzo and Y. Durocher, Biotinylation of the Fcγ receptor ectodomains by mammalian cell co-transfection: application to the development of a surface plasmon resonance-based assay, *J. Mol. Recognit.*, 2016, **29**, 60–69, DOI: 10.1002/JMR.2495.

26 C. Forest-Nault, J. Gaudreault, O. Henry, Y. Durocher and G. D. Crescenzo, On the Use of Surface Plasmon Resonance

 This journal is © The Royal Society of Chemistry 2026

Biosensing to Understand IgG-FcγR Interactions, *Int. J. Mol. Sci.*, 2021, **22**, 6616, DOI: 10.3390/IJMS22126616.
27 C. Orlandi, D. Deredge, K. Ray, N. Gohain, W. Tolbert, A. L. DeVico, P. Wintrode, M. Pazgier and G. K. Lewis, Antigen-Induced Allosteric Changes in a Human IgG1 Fc Increase Low-Affinity Fcγ Receptor Binding, *Structure*, 2020, **28**, 516–527, DOI: 10.1016/j.str.2020.03.001.
28 G. Dekkers, A. E. H. Bentlage, R. Plomp, R. Visser, C. A. M. Koeleman, A. Beentjes, J. Y. Mok, W. J. E. van Esch, M. Wuhrer, T. Rispens and G. Vidarsson, Conserved FcγR- glycan discriminates between fucosylated and afucosylated IgG in humans and mice, *Mol. Immunol.*, 2018, **94**, 54–60, DOI: 10.1016/J.MOLIMM.2017.12.006.
29 J. Zhao, R. Nussinov and B. Ma, Antigen binding allosterically promotes Fc receptor recognition, *MAbs*, 2019, **11**, 58–74, DOI: 10.1080/19420862.2018.1522178.
30 G. Dekkers, L. Treffers, R. Plomp, A. E. H. Bentlage, M. de Boer, C. A. M. Koeleman, S. N. Lissenberg-Thunnissen, R. Visser, M. Brouwer, J. Y. Mok, H. Matlung, T. K. van den Berg, W. J. E. van Esch, T. W. Kuijpers, D. Wouters, T. Rispens, M. Wuhrer and G. Vidarsson, Decoding the human immunoglobulin G-glycan repertoire reveals a spectrum of Fc-receptor- and complement-mediated-effector activities, *Front. Immunol.*, 2017, **8**, 279269, DOI: 10.3389/FIMMU.2017.00877/BIBTEX.
31 S. Zou, G. Peng and Z. Ma, Surface-Functionalizing Strategies for Multiplexed Molecular Biosensing: Developments Powered by Advancements in Nanotechnologies, *Nanomaterials*, 2024, **14**, 2014, DOI: 10.3390/NANO14242014.
32 R. M. Lubken, A. M. De Jong and M. W. J. Prins, Multiplexed Continuous Biosensing by Single-Molecule Encoded Nanoswitches, *Nano Lett.*, 2020, **20**, 2296–2302, DOI: 10.1021/ACS.NANOLETT.9B04561/SUPPL_FILE/NL9B04561_SI_002.MP4.
33 S. Zhang, Y. Zhang, J. Jiang, M. Charconnet, Y. Peng, L. Zhang and C. H. Lawrie, Shape-Specific Gold Nanoparticles for Multiplex Biosensing Applications, *ACS Omega*, 2024, **9**, 37163–37169, DOI: 10.1021/ACSOMEGA.4C04385.
34 A. Lučiūnaitė, K. Mašalaitė, I. Plikusiene, V. Maciulis, S. Juciute, M. Norkienė and A. Žvirblienė, Structural properties of immune complexes formed by viral antigens and specific antibodies shape the inflammatory response of macrophages, *Cell Biosci.*, 2024, **14**, 1–21, DOI: 10.1186/S13578-024-01237-1.
35 V. Maciulis, A. Lučiūnaitė, M. Usvaltas, S. Juciute, A. Ramanaviciene and I. Plikusiene, The second life for unused COVID-19 vaccines: Towards biosensing application, *Talanta*, 2025, **287**, 127647, DOI: 10.1016/j.talanta.2025.127647.
36 M. Usvaltas, V. Maciulis, A. Kausaite-Minkstimiene, I. Plikusiene and A. Ramanaviciene, Integrated optical and acoustic detection of SARS-CoV-2 spike anti-RBD antibodies using secondary antibodies and gold nanoparticles, *Talanta*, 2026, **298**, 128778, DOI: 10.1016/j.talanta.2025.128778.
37 I. Plikusiene, V. Maciulis, V. Vertelis, S. Juciute, S. Balevicius, A. Ramanavicius, J. Talbot and A. Ramanaviciene, Revealing the SARS-CoV-2 Spike Protein and Specific Antibody Immune Complex Formation Mechanism for Precise Evaluation of Antibody Affinity, *Int. J. Mol. Sci.*, 2023, **24**, 13220, DOI: 10.3390/IJMS241713220.
38 I. Plikusiene, V. Maciulis, A. Ramanaviciene, Z. Balevicius, E. Buzavaite-Verteliene, E. Ciplys, R. Slibinskas, M. Simanavicius, A. Zvirbliene and A. Ramanavicius, Evaluation of kinetics and thermodynamics of interaction between immobilized SARS-CoV-2 nucleoprotein and specific antibodies by total internal reflection ellipsometry, *J. Colloid Interface Sci.*, 2021, **594**, 195–203, DOI: 10.1016/j.jcis.2021.02.100.
39 Z. Balevicius, J. Talbot, L. Tamosaitis, I. Plikusiene, A. Stirke, G. Mickiene, S. Balevicius, A. Paulauskas and A. Ramanavicius, Modelling of immunosensor response: the evaluation of binding kinetics between an immobilized receptor and structurally-different genetically engineered ligands, *Sens. Actuators, B*, 2019, **297**, 126770, DOI: 10.1016/J.SNB.2019.126770.
40 J. Ahmad, J. Jiang, L. F. Boyd, A. Zeher, R. Huang, D. Xia, K. Natarajan and D. H. Margulies, Structures of synthetic nanobody–SARS-CoV-2–RBD complexes reveal distinct sites of interaction and recognition of variants, *J. Biol. Chem.*, 2021, **297**, 101202, DOI: 10.21203/RS.3.RS-625642/V1.
41 J. D. Walter, M. Scherer, C. A. J. Hutter, A. A. Garaeva, I. Zimmermann, M. Wyss, J. Rheinberger, Y. Ruedin, J. C. Earp, P. Egloff, M. Sorgenfrei, L. M. Hürlimann, I. Gonda, G. Meier, S. Remm, S. Thavarasah, G. van Geest, R. Bruggmann, G. Zimmer, D. J. Slotboom, C. Paulino, P. Plattet and M. A. Seeger, Biparatopic sybodies neutralize SARS–CoV–2 variants of concern and mitigate drug resistance, *EMBO Rep.*, 2022, **23**, e54199, DOI: 10.15252/EMBR.202154199.
42 S. Mandrekar, Q. Jiang, C. Y. D. Lee, J. Koenigsknecht-Talboo, D. M. Holtzman and G. E. Landreth, Microglia mediate the clearance of soluble Abeta through fluid phase macropinocytosis, *J. Neurosci.*, 2009, **29**, 4252–4262, DOI: 10.1523/JNEUROSCI.5572-08.2009.
43 F. Carbone, C. Russo, A. Colamatteo, C. L. Rocca, C. Fusco, A. Matarese, C. Procaccini and G. Matarese, Cellular and molecular signaling towards T cell immunological self-tolerance, *J. Biol. Chem.*, 2024, **300**, 107134, DOI: 10.1016/j.jbc.2024.107134.
44 S. Chen, A. F. U. H. Saeed, Q. Liu, Q. Jiang, H. Xu, G. G. Xiao, L. Rao and Y. Duo, Macrophages in immunoregulation and therapeutics, *Signal Transduction Targeted Ther.*, 2023, **8**, 1–35, DOI: 10.1038/s41392-023-01452-1.
45 A. Julià, I. Bonafonte-Pardàs, A. Gómez, M. López-Lasanta, M. López-Corbeto, S. H. Martínez-Mateu, J. Lladós, I. Rodríguez-Nunez, R. M. Myers and S. Marsal, Targeting of the CD80/86 proinflammatory axis as a therapeutic strategy to prevent severe COVID-19, *Sci. Rep.*, 2021, **11**, 11462, DOI: 10.1038/S41598-021-90797-0.

46 L. Grosche, I. Knippertz, C. König, D. Royzman, A. B. Wild, E. Zinser, H. Sticht, Y. A. Muller, A. Steinkasserer and M. Lechmann, The CD83 Molecule - An Important Immune Checkpoint, *Front. Immunol.*, 2020, **11**, 721, DOI: 10.3389/FIMMU.2020.00721.

47 K. Peckert-Maier, P. Langguth, A. Strack, L. Stich, P. Mühl-Zürbes, C. Kuhnt, C. Drassner, E. Zinser, M. Wrage, J. Mattner, A. Steinkasserer, D. Royzman and A. B. Wild, CD83 expressed by macrophages is an important immune checkpoint molecule for the resolution of inflammation, *Front. Immunol.*, 2023, **14**, 1085742, DOI: 10.3389/FIMMU.2023.1085742.

48 V. Cecchinato, V. Martini, E. Pirani, E. Ghovehoud and M. Uguccioni, The chemokine landscape: one system multiple shades, *Front. Immunol.*, 2023, **14**, 1176619, DOI: 10.3389/FIMMU.2023.1176619.

49 A. Mantovani, A. Sica, S. Sozzani, P. Allavena, A. Vecchi and M. Locati, The chemokine system in diverse forms of macrophage activation and polarization, *Trends Immunol.*, 2004, **25**, 677–686, DOI: 10.1016/j.it.2004.09.015.

50 P. Ruytinx, P. Proost, J. Van Damme and S. Struyf, Chemokine-Induced Macrophage Polarization in Inflammatory Conditions, *Front. Immunol.*, 2018, **9**, 1930, DOI: 10.3389/FIMMU.2018.01930.

51 H. Saada, Q. Pagneux, J. Wei, L. Live, A. Roussel, A. Dogliani, L. D. Morini, I. Engelmann, E. K. Alidjinou, A. S. Rolland, E. Faure, J. Poissy, J. Labreuche, G. Lee, P. Li, G. Curran, A. Jawhari, J. A. Yunda, S. Melinte, A. Legay, J. L. Gala, D. Devos, R. Boukherroub and S. Szunerits, Sensing of COVID-19 spike protein in nasopharyngeal samples using a portable surface plasmon resonance diagnostic system, *Sens. Diagn.*, 2022, **1**, 1021–1031, DOI: 10.1039/D2SD00087C.

52 S. Nair, Y. Jiang, I. S. Marchal, E. Chernobelsky, H. W. Huang, S. Suh, R. Pan, X. P. Kong, H. D. Ryoo and E. M. Sigurdsson, Anti-tau single domain antibodies clear pathological tau and attenuate its toxicity and related functional defects, *Cell Death Dis.*, 2024, **15**, 1–14, DOI: 10.1038/s41419-024-06927-9.

53 T. A. Bates, S. K. Gurmessa, J. B. Weinstein, M. Trank-Greene, X. H. Wrynla, A. Anastas, T. W. Anley, A. Hinchliff, U. Shinde, J. E. Burke and F. G. Tafesse, Biolayer interferometry for measuring the kinetics of protein-protein interactions and nanobody binding, *Nat. Protoc.*, 2025, **20**, 861–883, DOI: 10.1038/S41596-024-01079-8.

54 L. Han, R. Peng, W. Jiang, T. Xu, C. Zhang, K. Chen, Y. Zhang, H. Song and L. Jia, Coordination-driven reversible surfaces with site-specifically immobilized nanobody for dynamic cancer cell capture and release, *J. Mater. Chem. B*, 2020, **8**, 7511–7520, DOI: 10.1039/D0TB00574F.

55 V. Bobkov, A. M. Zarca, A. Van Hout, M. Arimont, J. Doijen, M. Bialkowska, E. Toffoli, A. Klarenbeek, B. van der Woning, H. J. van der Vliet, T. Van Loy, H. de Haard, D. Schols, R. Heukers and M. J. Smit, Nanobody-Fc constructs targeting chemokine receptor CXCR4 potently inhibit signaling and CXCR4-mediated HIV-entry and induce antibody effector functions, *Biochem. Pharmacol.*, 2018, **158**, 413–424, DOI: 10.1016/J.BCP.2018.10.014.

56 M. Qasemi, M. Behdani, M. A. Shokrgozar, V. Molla-Kazemiha, H. Mohseni-Kuchesfahani and M. Habibi-Anbouhi, Construction and expression of an anti-VEGFR2 Nanobody-Fc fusionbody in NS0 host cell, *Protein Expr. Purif.*, 2016, **123**, 19–25, DOI: 10.1016/J.PEP.2016.03.004.

57 K. R. Patel, J. T. Roberts and A. W. Barb, Multiple Variables at the Leukocyte Cell Surface Impact Fc γ Receptor-Dependent Mechanisms, *Front. Immunol.*, 2019, **10**, 223, DOI: 10.3389/FIMMU.2019.00223/FULL.

58 W. Wang and Q. Chen, Antigen improves binding of IgGs to FcγRs in SPR analysis, *Anal. Biochem.*, 2022, **640**, 114411, DOI: 10.1016/J.AB.2021.114411.

59 R. A. Robinett, N. Guan, A. Lux, M. Biburger, F. Nimmerjahn and A. S. Meyer, Dissecting FcγR Regulation through a Multivalent Binding Model, *Cell Syst.*, 2018, **7**, 41–48, DOI: 10.1016/j.cels.2018.05.018.

60 M. H. Bakalar, A. M. Joffe, E. M. Schmid, S. Son, M. Podolski and D. A. Fletcher, Size-Dependent Segregation Controls Macrophage Phagocytosis of Antibody-Opsonized Targets, *Cell*, 2018, **174**, 131–142, DOI: 10.1016/J.CELL.2018.05.059.

61 B. Azzarone, N. Landolina, F. R. Mariotti, L. Moretta and E. Maggi, Soluble SARS-CoV-2 Spike glycoprotein: considering some potential pathogenic effects, *Front. Immunol.*, 2025, **16**, 1616106, DOI: 10.3389/FIMMU.2025.1616106/BIBTEX.

62 X. Cao, Y. Tian, V. Nguyen, Y. Zhang, C. Gao, R. Yin, W. Carver, D. Fan, H. Albrecht, T. Cui and W. Tan, Spike protein of SARS-CoV-2 activates macrophages and contributes to induction of acute lung inflammation in male mice, *FASEB J.*, 2021, **35**, e21801, DOI: 10.1096/FJ.202002742RR.

63 K. Peckert-Maier, A. B. Wild, L. Sprißler, M. Fuchs, P. Beck, J. P. Auger, P. Sinner, A. Strack, P. Mühl-Zürbes, N. Ramadan, M. Kunz, G. Krönke, L. Stich, A. Steinkasserer and D. Royzman, Soluble CD83 modulates human-monocyte-derived macrophages toward alternative phenotype, function, and metabolism, *Front. Immunol.*, 2023, **14**, 1293828, DOI: 10.3389/FIMMU.2023.1293828.

64 P. Langguth, K. Peckert-Maier, P. Beck, C. Kuhnt, C. Draßner, A. Deinzer, A. Steinkasserer and A. B. Wild, CD83 acts as immediate early response gene in activated macrophages and exhibits specific intracellular trafficking properties, *Biochem. Biophys. Res. Commun.*, 2023, **647**, 37–46, DOI: 10.1016/J.BBRC.2023.01.069.

65 M. H. Luo, W. Zhang, J. Yang, X. Du, X. Wang, G. Xu, H. Tang, Z. Wang, X. Zhong, J. Feng and N. Ma, CD83 mediates the inhibitory effect of the S1PR1 agonist CYM5442 on LPS-induced M1 polarization of macrophages through the ERK-STAT-1 signaling pathway, *Int. Immunopharmacol.*, 2024, **143**, 113526, DOI: 10.1016/j.intimp.2024.113526.

 This journal is © The Royal Society of Chemistry 2026